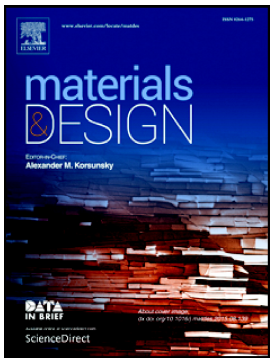

Investigation of additive incorporation on rheological, microstructural and mechanical properties of 3D printable alkali-activated materials

Mehdi Chougan, Seyed Hamidreza Ghaffar, Pawel Sikora, Sang-Yeop Chung, Teresa Rucinska, Dietmar Stephan, Abdulrahman Albar, Mohammad Rafiq Swash

PII: S0264-1275(21)00127-1

DOI: https://doi.org/10.1016/j.matdes.2021.109574

Reference: JMADE 109574

To appear in: *Materials & Design*

Received date: 29 November 2020

Revised date: 27 January 2021

Accepted date: 6 February 2021

Please cite this article as: M. Chougan, S.H. Ghaffar, P. Sikora, et al., Investigation of additive incorporation on rheological, microstructural and mechanical properties of 3D printable alkali-activated materials, *Materials & Design* (2021), https://doi.org/10.1016/j.matdes.2021.109574

Investigation of additive incorporation on rheological, microstructural and mechanical properties of 3D printable alkali-activated materials

Mehdi Chougan[a], Seyed Hamidreza Ghaffar[a,*] Seyed.Ghaffar@brunel.ac.uk, Pawel Sikora[b,c], Sang-Yeop Chung[d], Teresa Rucinska[c], Dietmar Stephan[b], Abdulrahman Albar[e], Mohammad Rafiq Swash[e]

[a]Department of Civil and Environmental Engineering, Brunel University London, Uxbridge, UB8 3PH, United Kingdom

[b]Building Materials and Construction Chemistry, Technische Universität Berlin, Gustav-Meyer-Allee 25, 13355 Berlin, Germany

[c]Faculty of Civil Engineering and Architecture, West Pomeranian University of Technology, Szczecin, Al. Piastow 50, 70-311 Szczecin, Poland

[d]Department of Civil and Environmental Engineering, Sejong University, 209 Neungdong-ro, Gwangjin-gu, Seoul 05006, Republic of Korea

[e]Department of Electronic and Electrical Engineering, Brunel University London, Uxbridge, UB8 3PH, United Kingdom
[*]Corresponding Author:

Abstract

This study investigates the addition of Poly-vinyl Alcohol (PVA) fibres and attapulgite nanoclay to alkali-activated materials (AAMs) with the aim of enhancing the mechanical performance and optimizing the printability and buildability of AAMs. The fresh properties of six mix formulations, including flowability, slump values, rheology, shape retention, and extrusion window, were evaluated. The best performing mixes, that exhibited optimal fresh properties, were 3D printed, and their mechanical performance, microstructure, and buildability were investigated. The addition of 1 wt.-% attapulgite nanoclay (i.e. A-1) showed the desirable fresh properties required for 3D printing, as well as providing sufficient mechanical reinforcement to the samples. The 3D printed A-1 samples showed an improved flexural and compressive strength by 43% and 20%, respectively, compared to both the casted and printed control mixes. Moreover, microstructure analysis, including SEM, Rapidair measurement, and micro-CT, provided evidence of the compatibility by showing the lowest pores anisotropy and mixture homogeneity, between attapulgite and AAMs.

Key words: Alkali-activated materials (AAMs), Attapulgite nanoclay, Poly-vinyl Alcohol (PVA) fibres, 3D printing, Rheology, RapidAir measurement, Micro-CT, Reinforcement

1. Introduction

The application of alkali-activated materials (AAMs) has been expanded by employing additive manufacturing (AM) technology [1]. The implementation of these materials with high mechanical performance and adjustable setting time

provides an excellent feedstock for 3D printing [2,3]. Besides the mechanical strength, the interaction between particles, particle size, shape and gradation can all influence a mix in terms of printability (e.g. optimized extrusion, shape stability and complex shape buildability) [4,5]. Fresh property investigations and optimizations are still vital to obtain a 3D printable cementitious composite mixture. Various types of industrial products and by-products, such as ground granulated blast-furnace slag (GGBS), fly ash (FA), silica fume (SF), and metakaolin [6,7] have been used as aluminosilicate source binder. On the other hand, variety of activator solutions, including potassium hydroxide, potassium silicate, sodium silicate, sodium metasilicate, sodium sulfate, and sodium hydroxide solutions in different ratios are employed to start the polycondensation reaction, which alters both the fresh and hardened properties which should work towards a practical mix design for successful 3D printing [8–10]. Recent studies are still slow to maximize the full potential of AAMs in 3D printing, and many are using them as partial replacements to ordinary Portland cement (OPC) in the binder, solely for the small contribution to the environmentally friendliness. However, rheology modifier agents and reinforcement additives (e.g. polyvinyl alcohol (PVA), polypropylene (PP) [11], polyethylene (PE) [12], attapulgite [13], and nano-graphite particles (NGP) [14] have improved the printability and mechanical performance of 3D printed AAMs objects leading to more streamlined larger scale projects. Alkali-activated mixes being implemented in 3D printing processes should be flowable enough to be pumped and extruded through a nozzle, as well as gain sufficient strength and stiffness to retain its shape after layer by layer deposition [15]. In general, the most critical challenge in the fresh property adjustment for 3D printing is to develop a mix with the high shear yield stress and low viscosity [7]. It is well accepted by several authors that the colloidal interactions, contact forces, and hydrodynamic forces between the AAMs particles are able to induce a thixotropy phenomenon, which indicates the different behaviour of mixes under the shear force and at resting time (i.e. low viscosity of fresh paste when subjected to shear force and high viscosity at the resting time) [16,17]. Several methods, including rheology, flowability, extrusion window, and mini-slump tests, have been proposed by researchers to better understand the thixotropic behaviour of AAMs reinforced with micro and nano additives [14]. Nematollahi et al. (2018), reported that the inclusion of different types of fibres, including PP, PVA, and polyphenylene benzobisoxazole (PBO) in the geopolymer increased the flexural strength. However, the interlayer bonding between the printed layers decreased [11]. Similar trends were also reported by the same authors, in which the incorporation of PP fibres reduced the spread diameter of fresh geopolymer and induced the positive effect on the compressive strength of hardened parts in the perpendicular load direction [18]. Panda et al. (2017) also focused on 3D printing of geopolymer incorporated with glass fibre (GF) inclusion up to 1 wt.-% and found a proportional increase in flexural, tensile, and compressive strength [19]. Furthermore, Panda et al. (2019) also found that thixotropic behaviour of geopolymers increased with incorporation of 0.5 wt.-% attapulgite nano-clay, which resulted in the improved printability due to the high shear stress and low viscosity of the fresh mixture. However, the mixes with nano-clay exhibit lower compressive strength compared to neat geopolymer [20]. The incorporation of nano-clays is effective because of the low thickness of individual platelets (i.e. 1 nm) and high lateral dimensions ranging from 200 nm to

2000 nm. This resulted in a high aspect ratio making nano-clays highly reactive [21]. In line with the aforementioned results and author's previous works [14,22], the fresh property investigation proved to be an effective and useful tool for identifying the suitable mix in terms of both mechanical property and printability. Therefore, in this study, PVA fibre with the dosages of 0.25 wt.-% and 0.5 wt.-%, attapulgite nano-clay with the dosages of 0.5 wt.-% and 1 wt.-%, and a combined mix composed of 0.25 wt.-% of PVA and 1 wt.-% of attapulgite have been added to the alkali-activated mixture. All the mixtures were characterized via fresh property tests, including flowability, rheology, mini slump, extrudable window, shape retention, and buildability. The chosen mixtures were then printed and investigated in the hardened state to evaluate the effect of additives on microstructure (i.e. SEM, RapidAir measurement, and μ-CT) and mechanical properties (i.e. flexural strength, and compressive strength). Finally, the correlation between fresh properties and mechanical performance was examined.

2. Materials and experimental testing methods

Outlined **Figure 1** is the comprehensive framework of all the mix design and experimental procedures employed in this study.

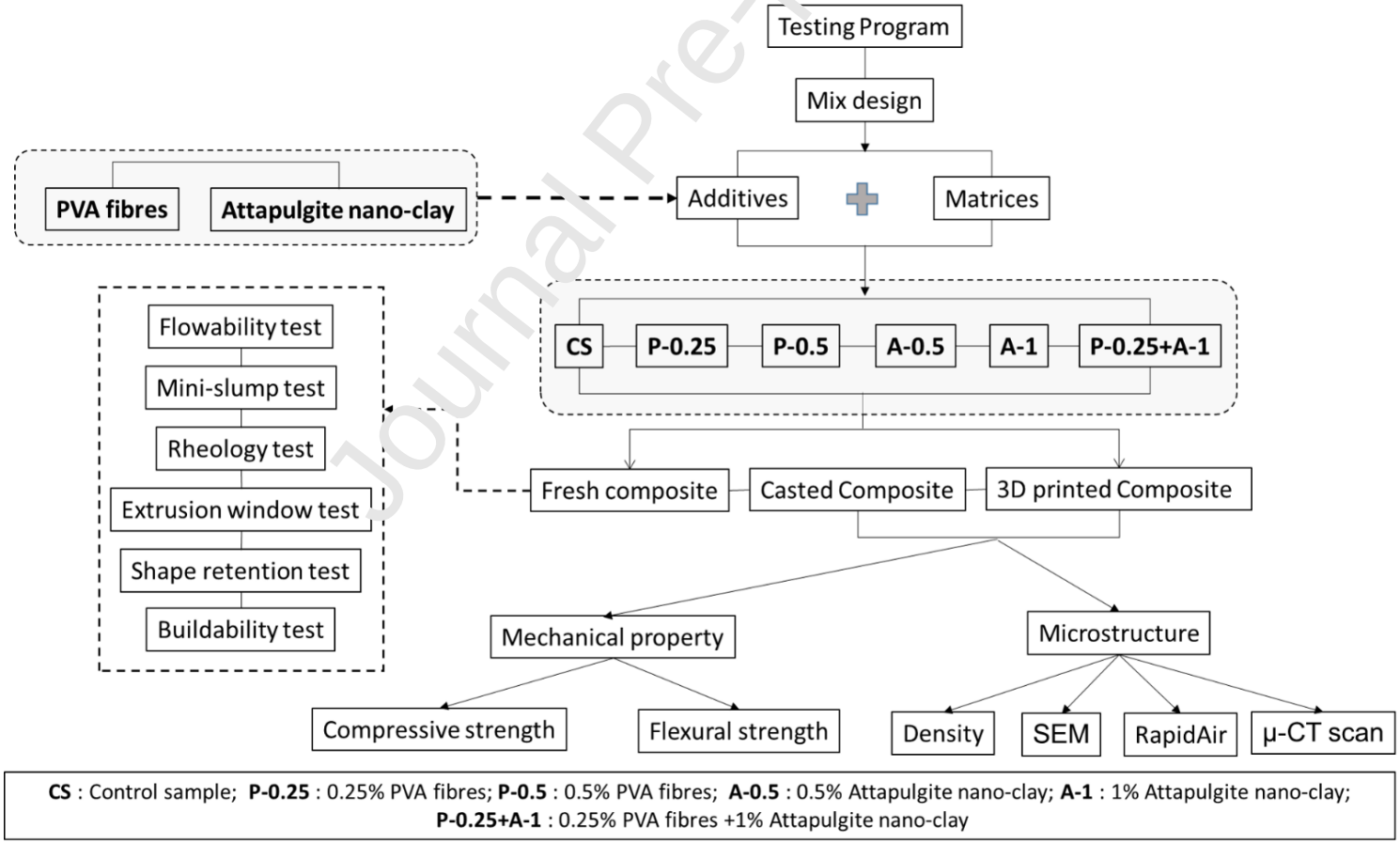

Figure 1 – Experimental design and analysis framework

2.1 Materials

According to the author's previous study [14], the most effective alkali-activated cementitious composite for 3D printing was composed of (i) fly ash (Cemex, UK) which meets normal fineness (N) Category of British standard BS EN 450-1:2012. The bulk density of fly ash is ranged between 0.8 - 1.0 g/cm^3 with the maximum permitted residue of 40% on a 45 µm sieve in dry state, (ii) ground-granulated blast furnace slag (Hanson Heidelberg Cement, UK) which complies with EN15167-1 with the bulk density of approximately 2.4 - 3 g/cm³ (20 °C). D50 and D90 percentiles of 17.3 µm and 49.27 µm, respectively, were registered for this product. More details on the material characterizations, including the material size distribution and compositions, can be found in previous researches [23,24], (iii) micro-silica fume (J. Stoddard & Sons Ltd), (iv) graded sand including two different sand sizes of 0-0.5mm and 0.5-1.0mm following BS EN 410-1:2000, (v) sodium silicate solution with the SiO_2/Na_2O mass ratio of 3.23 (Solvay SA, Portugal), and (vi) 10 mol/l sodium hydroxide solution (Fisher Scientific, Germany). Polyvinyl Alcohol (PVA) fibres (**Figure 2a** and **Table 1**) provided by (Jesmonite, UK), and attapulgite nano-clay (**Figure 2b**) supplied by (Attagel 350, Lawrence Industries Ltd, UK) were incorporated as a reinforcement and thixotropic modifier additives, respectively. As indicated in Figure 2b, attapulgite nano-clay particles have an angular shape with sharp edges. Based on the data provided by the supplier, the material has a bulk density of 0.769 g/cm³ and maximum permitted residue of 45% on a 44µm sieve in a dry state.

Table 1 – Technical data on poly-vinyl alcohol fibre

Fibre	Diameter (µm)	Length (mm)	Aspect Ratio	Young's Modulus (GPa)	Elongation at Rupture (%)	Density (kg/m^3)	Nominal Strength (MPa)
PVA	150	12	80	25-41	6	1300	1000

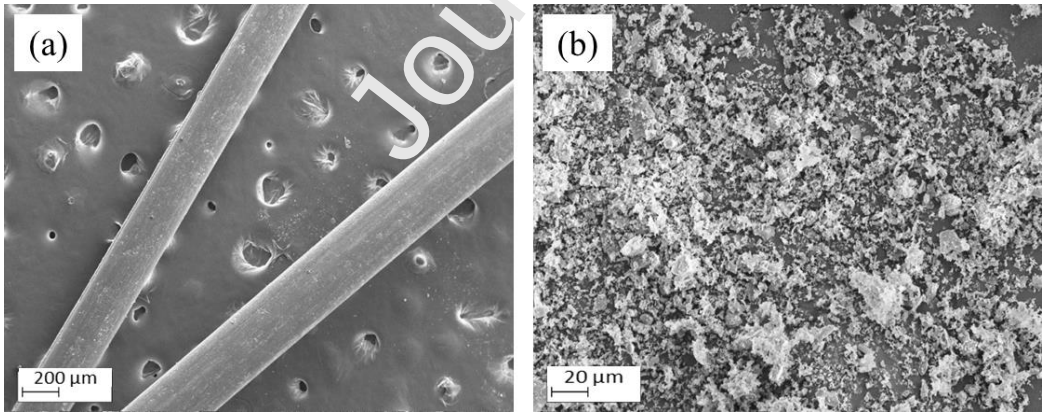

Figure 2 – Microstructure of (a) PVA fibre and (b) Attapulgite nano-clay

2.2 Mixing procedure and sample preparations

As shown in **Table 2**, a total of six alkali-activated mixes were produced. The FA, GGBS, and SF content were set to 60, 25, and 15 wt.-%, respectively, by the overall weight of the binder. Moreover, the activator solution dosage (i.e. NaOH+Na_2SiO_3) used was 40 wt.-% of the total weight of the binder. Two particle size ranges of 0 to 0.5 mm and 0.5 to 1 mm were obtained after oven-drying and sieving the fine river sand. The sand to binder ratio used in this study is 0.55. The alkali-activated cementitious composites were prepared in three separate stages. In the first stage, the precursor ingredients, i.e. binders (FA+GGBS+SF) and graded sand, were dry-mixed using a planetary mixer (Kenwood, Germany) for 2 min at 250 rpm. The additives (i.e. PVA fibres and attapulgite nano-clay) were slowly added to the dry-mixture and mixed for another 2 min at 250 rpm. The additives volume fractions have been chosen based on the previous studies conducted by Panda et al. (2019) [25] and Nematollahi et al. (2018) [11]. The alkali activators i.e., sodium hydroxide and sodium silicate solutions with the fixed mass ratio of 2:1 were mixed at 700 rpm for 5 min, and then gradually added to dry-mixture and stirred for 2.5 min at 250 rpm, followed by mixing at 450 rpm until a homogeneous alkali-activated mixture was achieved.

Table 2 – Mix design formulations with a constant water/solid ratio of 0.4

Name	Binder (wt.-%)			Additive (wt.-%) (of AAM)		Aggregate (wt.-%)		Na_2SiO_3: NaOH ratio (by weight)
	FA	GGBS	SF	PVA	Attapulgite nano-clay	0-0.5 mm	0.5-1 mm	
Control Sample (CS)	60	25	15	0	0	60	40	2:1
P-0.25	60	25	15	0.25	0	60	40	2:1
P-0.5	60	25	15	0.5	0	60	40	2:1
A-0.5	60	25	15	0	0.5	60	40	2:1
A-1	60	25	15	0	1	60	40	2:1
P-0.25+A-1	60	25	15	0.25	1	60	40	2:1

2.3 Printing setup

Similar to our previous works [14, 22], a gantry 3D printer equipped with a custom-designed auger extruder was utilized with a circular-shaped nozzle of size 20 mm, motion speed of 20 mm/s, and nozzle standoff of 10 mm. All the printable mix formulations were printed in a rectangular-shape and then cut to the 160 x 40 x 40 mm prisms (three samples for each composition) to keep it consistent with the casted samples.

2.4 Fresh properties assessment

Several test methods were used to obtain parameters which are interlinked and give evidence which explains the rheological properties of AAMs:

- Flow table test was assessed to determine the workability and consistency of fresh mixtures following the BS EN 1015- 3:1999. The flowability of the fresh mixtures was measured at 0 minutes, 5 minutes, and 15 minutes. In order to facilitate the comparison, the flowability percentage of each mixture was calculated using the following equation (see **Eq.1**):

$$FP = \left(\frac{d_{Average} - d_0}{d_0}\right) \times 100 \quad (1)$$

Where, FP is flow percentage, $d_{Average}$ is average spread-diameter of the paste in two perpendicular direction spread, and d_0 bottom cone diameter.

- The extrusion efficiency has been associated with an 'extrusion window', where a specific volume of material shows required workability to be extruded smoothly, without causing any discontinuity [26]. The extrusion efficiency test was conducted by printing a straight-lined filament of size 200mm in length. A filament was printed every 5 minutes rest-intervals from 0 minutes until the mix was no longer extrudable.
- The mini-slump test was also carried out to determine the workability or fluidity of the fresh alkali-activated composites as it is quantitatively related to the yield stress of fresh mixtures [27,28]. The experiment was performed under BS EN 12350-2:2009. Mini-slump cone apparatus used had the height, bottom, and top dimensions of 57, 38, and 19 mm, respectively. After one minute, the flow height reduction of each sample was recorded as slump value [28]. Moreover, the relative slump value was calculated according to the ASTM C1437 from the following equation (see **Eq.2**):

  $$\Gamma_P = \left(\frac{d}{d_0}\right)^2 - 1 \quad (2)$$

  Where, Γ_P is relative slump value, d is average spread-diameter of the paste in two perpendicular direction spread, and d_0 bottom cone diameter.

- The rheological behavior of fresh alkali activated mixtures was evaluated by employing KinexusLab + rheometer (Malvern Instruments Ltd., UK) in a parallel-plate configuration equipped with the rSpace software (Malvern Panalytical Ltd, UK). The tests were conducted immediately after the mixing procedure under the shear rate between 0.1 s^{-1} and 30 s^{-1} over 18 speed intervals, and the flow curves were plotted. All the rheology tests were performed at an ambient temperature (i.e. constant 25 °C). Three replications were conducted to verify the repeatability of rheology tests. Due to the pseudoplastic behaviour and non-Newtonian nature of fresh alkali-activated mixtures, the Herschel–Bulkley fitting model (see **Eq.3**) was adopted to fit the flow curves accurately and to evaluate the yield shear stress.

$$\tau = \tau_0 + K\dot{\gamma}^n \quad (3)$$

Where, τ is shear stress, τ_0 is yield stress, K is consistency, $\dot{\gamma}$ is shear rate, and n is flow index.

- The shape retention of each mix was examined based on our previous methodology [14]. Six layers of each mixture were printed. After adequate resting time, high-quality footages of the printed samples were taken, and quantitative measurement was carried out by employing ImageJ software to determine the accurate height of each deposited layer.

2.5 Mechanical property assessment

The flexural and compressive strength tests were conducted on the casted and printed prismatic samples with dimensions of 160 × 40 × 40mm^3. The mechanical property tests were carried out after seven days of curing in which for the first 24 hours, the samples were placed in the oven at 60°C [29] and the remaining six days air-cured. These tests conformed to BS EN 196-1:2016 and were completed using an Instron 5960 Series Universal Testing System.

2.6 Microstructure analysis

A small cross-section of the printed samples was cut using broken portions of samples in flexural strength test to investigate the microstructure using SEM (Supra 35VP, Carl Zeiss, Germany) coupled with Energy dispersive spectroscopy (EDS) analyser (EDAX, U.S.A). Prior to the SEM analysis of each composition, a minimum number of ten specimens with the approximate size of 10 mm^3, were gold-coated by means of Edwards S150B sputter coater to provide electrical conductivity on samples surface.

2.6.1 RapidAir measurements and micro-computed tomography

In order to assess the microstructural characteristics of 3D printed specimens, two image-based approaches were applied: (i) 2D standardized technique based on a linear traverse method and (ii) X-ray micro-computed tomography (micro-CT) method enabling to obtain a 3D volumetric images of concretes. Our previous study showed that both techniques can be successfully applied to evaluate the microstructural properties of cementitious composites with satisfactory correlation between obtained results [30].

Figure 3 – Representation of specimen extraction zones used for RapidAir (yellow) and micro-CT (blue) measurements.

To evaluate the 2D air void characteristics of printed elements an automatic RapidAir 457 Automated-Air-Void-Analyzer (Concrete Experts International, Sweden) was used following ASTM C 457-90 “Standard Test Method for Microscopical Determination of Parameters of the Air-Void System in Hardened Concrete” and its corresponding European version EN 480-11 “Determination of air void characteristics in hardened concrete”. The device enables to perform the air void analysis with a resolution of 1 to 2.5 µm.

Specimens dedicated for this measurement were rectangular specimens with an approximate area of 96 cm², obtained from vertical cross sections of specimens (**Figure 3**). Prior to testing, cured concrete samples were cut into 1 cm-thick slices and one face of the sample was thoroughly polished. The surfaces of the samples were then painted with a black marker and zinc (II) oxide paste to increase the contrast between the air voids and the matrices. Two specimens were tested twice in each case following the BS EN 480-11 standard. The surface in question had an area of 120×80 mm^2. The RapidAir device enables to perform the air void analysis with a resolution of 1 to 2.5 µm. Two measurements of each specimen were performed and mean value was taken.

To assess the concrete characteristics along the height of specimen, three representative areas were defined: upper part, center part and lower part (**Figure 3**). X-ray micro-computed tomography (micro-CT) evaluations were performed on 20×20×20 mm^3 specimens cut out from the upper, middle, and lower part of each extraction zone of printed element. The used micro-CT device is SKYSCAN1172, ex-vivo at Seoul National University in South Korea.

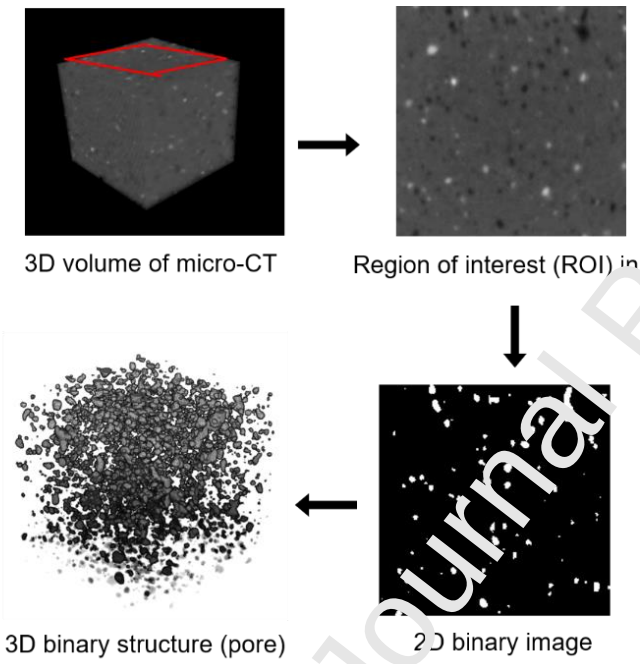

Figure 4 – Micro-CT imaging for visualizing pore structure (Note: in the 2D binary image, the white represents pores within the specimen, while the gray colored parts represent pores in 3D binary image. The sample has the dimension of 20×20×20 mm^3)

Figure 4 describes the imagining procedure. The main target of the use of micro-CT images is to investigate the pore structures of the specimens. It was demonstrated that pores within 3D printed materials tend to irregular or anisotropic compared to the pores in casted samples, as shown in **Figure 4**. In general, an originally reconstructed micro-CT image is expressed with 256 values (0-255, 8-bit) or 25536 values (0-25535, 16-bit). In this study, 8-bit images were used to visualize the pore structure within the printed specimens. To segment pores from the reconstructed 8-bit images, a proper threshold value was selected using Otsu method [31] as well as manual adjustment, and the image segmentation was conducted using the imaging toolbox in MATLAB (R2020a). Each image

was composed of 200x200 pixels with the 46.7 µm pixel size, and a 3D image was generated by subsequently stacking of the binarized images along the direction of height.

The anisotropy of the pore shape was confirmed using a probabilistic method, which is used to evaluate relative phase clustering size. Here, a probabilistic function, lineal-path function (L_2) [32,33], was used to investigate directional pore characteristics of the specimens. This function can be utilized to investigate and continuity of pores (L_2). Detailed descriptions of the used function can be found in [33,34], and general formulations are presented as follows (see **Eq.4**):

$$lim_{r\to 0}\, L_2(r,\theta,\emptyset) = f_v\,, lim_{r\to\infty}\, L_2(r,\theta,\emptyset) = 0 \qquad (4)$$

Where *r* is the distance between the two points, while θ and $\emptyset$ are the angle between the test line and the *z*-axis, and the angle between the projections of the test line on the *xy*-plane, respectively. f_v denotes the pore volume fraction. Using the L_2 function, the relative length along each direction can be compared. However, it is limited to be used for quantitative comparison because the feature of the L_2 function is a type of distribution. To overcome the limitation, the each graph was integrated, and the computed value was used as the index to compare the degree of anisotropy of pores in each specimen.

2.7 Buildability test

An ad hoc testing method was employed by printing 5500 g of alkali-activated fresh composite in a circular-shape printing path with a diameter of 150 mm. After the printing process, the quality of samples in terms of maximum height of printed objects, vertical distortion, and layer deformation was investigated visually. High-quality pictures of the printed samples were used to perform a visual investigation of each mix's buildability and outer-surface finish. ImageJ software was also employed to measure accurate reduction in bottom layers height and maximum printing height of each sample.

3. Results and discussion

3.1 Effect of additives incorporation on fresh properties

As reported by several authors, e.g. [7,35–37], the cement-based composites have the colloidal interaction and are considered as fully thixotropic, which is attributed to the presence of Van der Waals colloidal forces in the materials in the fresh state. This can lead to generating initial yield stress. However, because of the high-viscosity behaviour of potassium silicate chemical reagents within the alkali-activated cementitious composites, the hydrodynamic effect is presented in these materials [7]. Previously, attapulgite nano-clay [13] and PVA fiber [38] were incorporated to improve the thixotropic behaviour over the hydrodynamic effect in the alkali-activated mixtures. The attapulgite particle edges with the opposite electrical charge induce the electrical attraction between the particles to generate high yield stress at the resting stage. Incorporation of attapulgite with the fine particle size can form Van der Waals bonding within mixture by filling the gaps between binder components [25]. On the other hand, the electrostatic

bonding can be formed due to intermolecular interactions between the PVA's hydroxyl group (–OH) and cementitious binders' surfaces, improving the thixotropic behaviour in the fresh state [39].

Following the methodology specified in BS EN 1015- 3:1999, an initial flowability (i.e. 5 minutes) of 32% was recorded for the control sample (CS). As can be seen in **Figure 5**, the flowability of all PVA fibre-reinforced mixtures (i.e. P-0.25 and P-0.5) were reduced compared to the CS. The highest reduction of 26.5% was obtained by the 0.5% PVA sample. The presence of oxygen-containing functional groups (i.e. hydroxyl group -OH) on the outer surface of PVA fibers absorbs free water of the fresh mixture. This results in increased friction between the fibres and mixture's solid components making it stiffer compared to control sample [38,40]. As reported by Zhu et al. (2018), fiber type and fiber dosage are the most critical parameters affecting the flowability. They also reported that the PVA fiber incorporation accelerates the reaction kinetics of fresh mixtures at early ages, which was evidenced by increasing the reaction heat release rate during the activation process [41]. Moreover, the long PVA fibers (i.e. 12 mm) with the flexible nature can easily twist and ball together, forming an agglomerated aggregate within the mixture during the mixing procedure, which leads to a decrease in the flowability [42].

The inclusion of attapulgite nano-clay reduces the flowability compared to the CS (see **Figure 5**). However, the attapulgite incorporation shows a more considerable influence on decreasing the overall flowability than PVA fibre incorporation when compared to the control sample. The results revealed that the initial flowability was reduced by the addition of 0.5 wt.-% and 1 wt.-% of attapulgite (i.e. A-0.5 and A-1) and reached 18 % and 25 %, respectively. The hybrid mixture (i.e. P-0.25+A-1) also proved to be successful in increasing the cohesion of the resulted mixture, with an approximate initial flowability of 22%. The reduced flowability of mixtures containing attapulgite nano-clay can be attributed to the increased water absorption generated by the fine particle size and high specific surface area of attapulgite particles. Moreover, the better dispersion of nano-clay in lower dosage, i.e. 0.5 wt.-%, compared to 1 wt.-% leads to the better separation of nano-clay particles hence remarkably diminishing the flowability of the fresh mixture.

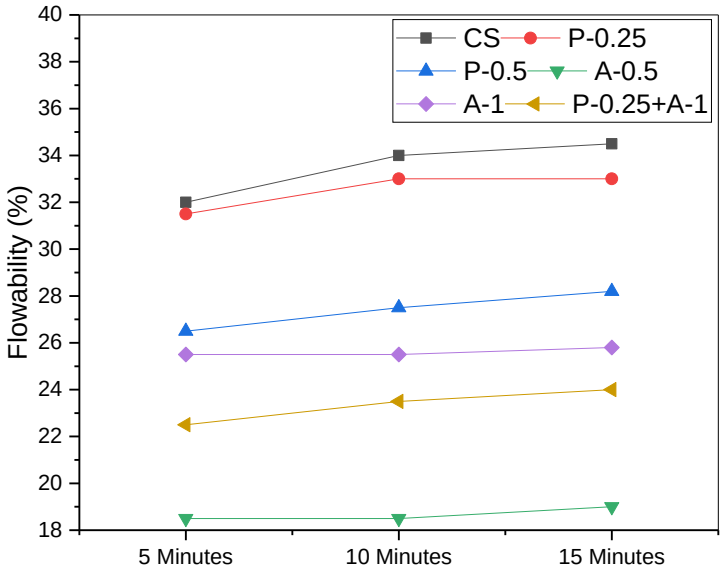

Figure 5 – Flowability of different alkali-activated materials

The yield shear stress of each fresh mixture with and without additive was determined. It is commonly known that the yield stress is related to the slump values (i.e. slump height and relative slump value) of an alkali-activated composite [28]. In general, higher yield stress and lower mini-slump values are found to be the required conditions for a printable mix formulation [10]. Therefore, the mini-slump test was also carried out for the analysis of the flow behaviour of the fresh mixtures to check workability and shape stability of the mix. The results show that the yield shear stress of alkali-activated mixture increased from 1216 Pa for the control sample to 1361 Pa and 1522 Pa for P-0.25 and P-0.5, respectively. As observed in **Figure 6a, b and Table 3**, the results obtained for yield stress are completely aligned with the values registered for mini-slump tests, where the addition of PVA fibres with the dosage of 0.25 wt.-% and 0.5 wt.-% have diminished the slump height by 14% and 43% and relative slump value by 33% and 37%, respectively, compared to the control sample. On the other hand, the addition of 0.5 wt.-% and 1 wt.-% attapulgite increased the yield stress, reaching 2785 Pa and 1797 Pa, respectively. In a good agreement with the rheology results, the slump values were also drastically reduced (i.e. 71% for slump height and 60% for relative slump value) by the incorporation of 0.5 wt.-% attapulgite. However, the addition of 1 wt.-% attapulgite increased the slump values which is comparable to that of control sample (i.e. slump height of 7 mm and relative slump of 0.38). The hybrid mix composed of PVA fiber and attapulgite (i.e. P-0.25+A-1) also indicated a remarkable decrease in yield shear stress, slump height and relative slump value by 55%, 57%, and 17%, respectively, compared to control sample's respective values.

The author's previous work and several other researches have confirmed the direct relation between extrusion window and the other fresh properties of alkali-activated composites [14,20,43]. Moreover, the results obtained from the extrusion window test are known as the most pertinent and relevant parameter among other fresh property factors as it exactly imitate the 3D printing process of fresh AAMs [44]. This is due to the fact that all the other properties of a mix are insignificant if the mix cannot be extruded [45]. Therefore, the impact of additive

incorporation on the extrusion window of alkali-activated mixtures in the fresh state was examined, and the results are depicted in **Figure 6b**. As can be seen in **Figure 6b**, the increase in PVA fiber dosage decreased the extrusion window of the mixture from 40 min for P-0.25 to 30 min for P-0.5. Comparing to CS (i.e. 35 min extrusion window), the samples with the lowest dosage of fibres (i.e. P-0.25) poses a 15% higher extrusion window. Increasing the attapulgite dosage, however, followed a reverse trend in which the extrusion window increased from 10 min for A-0.5 to 20 min for A-1. Moreover, the hybrid mix that contained the highest ratio of attapulgite and lowest dosage of PVA fibres (i.e. P-0.25+A-1) had an equal extrusion window (i.e. 20 min) compared to the A-1 composition. In all compositions except P-0.25, the inclusion of additives diminished the extrusion window compared to CS.

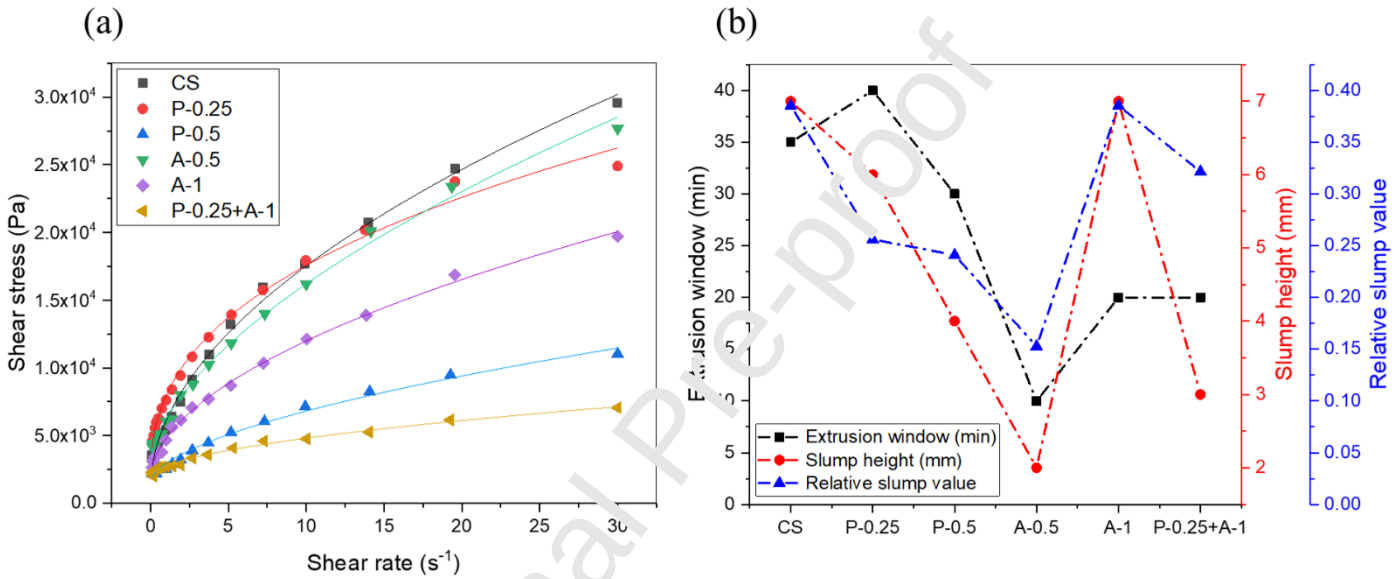

Figure 6 – Fresh properties of samples: (a) rheology measurements, (b) extrusion window and slump values (b is a bit too hard to understand but leave it if you think is okay)

Table 3 – Rheological properties of samples with different additives

Sample	Yield stress (Pa)	K (Pa.s^n)	n	R^2
CS	1215.62	4899.68	0.522	0.9959
P-0.25	1361.18	6594.87	0.390	0.9934
P-0.5	1521.64	1410.51	0.574	0.9915
A-0.5	2785.08	3431.80	0.592	0.9959
A-1	1797.11	3003.99	0.503	0.9974
P-0.25+A-1	1889.60	856.90	0.530	0.9901

The shape retention of all the samples were measured, and the results are shown in **Figure 7**. Among all samples, the mixture with 0.5 wt.-% of attapulgite (i.e. A-0.5) was excluded since it was not printable, as previously confirmed by the considerably low fresh property efficiency, including flowability, yield stress, slump values, and extrusion window, that was out of the employed operating extrusion system's limit. For the printable mixtures, the results of the shape

retention were compared in terms of first layer's height (H_1) and the height difference between the first and the sixth printed layer (H_{dif}).

The results indicate that the H_1 and H_{dif} values for the sample with 1 wt.-% attapulgite particles (i.e. A-1) was improved and reached 6.3 mm and 5.9 mm, compared to the values obtained for CS (i.e. 5 mm and 6.3 mm). The increased dosage of PVA fibres also improved the shape retention of the layers. The H_1 value of P-0.25 and P-0.5 was increased by 20% and 90%, respectively, which was higher than that of CS. The H_{dif}, on the other hand, was decreased from 6.3 mm for CS to 6.1 mm and 3.5 mm for P-0.25 and P-0.5, respectively. The results suggest that the incorporation of PVA in high dosages (i.e. 0.5 wt.%) is more effective in terms of shape-stability during the deposition of the subsequent layers. The same effect was also observed for P-0.25+A-1 in which H_1 and H_{dif} reached 7.3 and 5.0 mm, respectively. However, the visual observations on the upper layers' quality showed a considerable inconsistency, which was generated due to the lower performance of the aforementioned mixes in terms of slump height, extrusion window, and yield stress compared to the CS and the mix with a lower fibre dosage (i.e. 0.25 wt.-%).

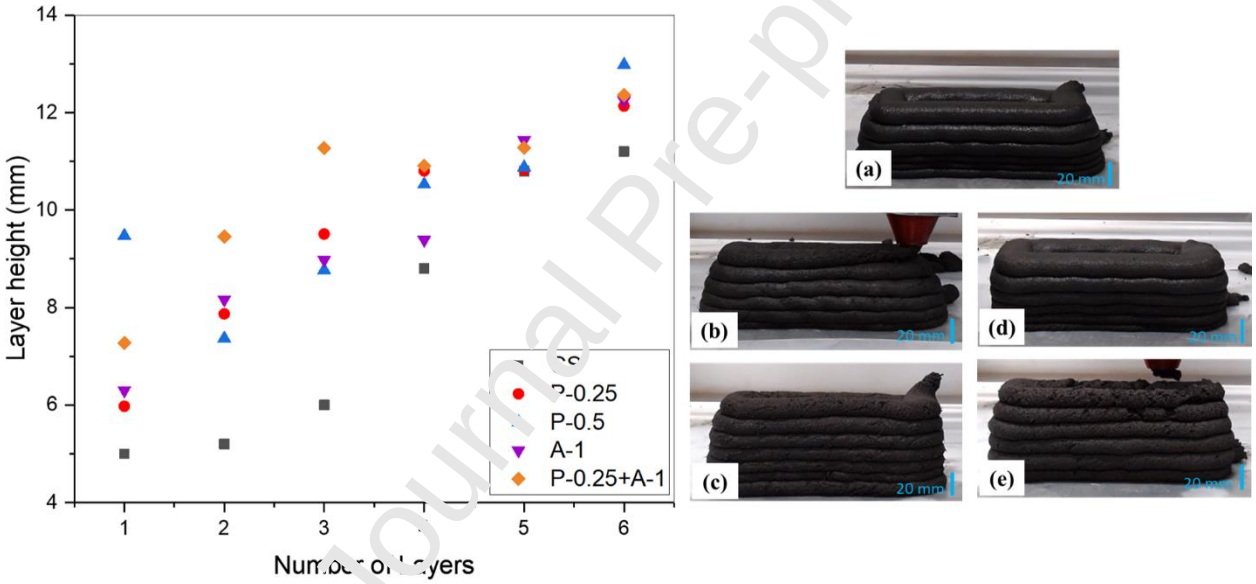

Figure 7 – Shape retention results and printing appearance of the printed samples, (a) control sample, (b) P-0.25, (c) P-0.5, (d) A-1, (e) P-0.25+A-1

3.2 Effect of additives incorporation on mechanical properties

The mechanical performance of alkali-activated composites has been investigated to identify the ideal printable mixes to be used as feasible feedstock for the eventual upscaling process. **Figures 8a-c** shows comparisons between 3D printed and conventionally casted specimens in a perpendicular load direction in terms of density, flexural, and compressive strength, respectively.

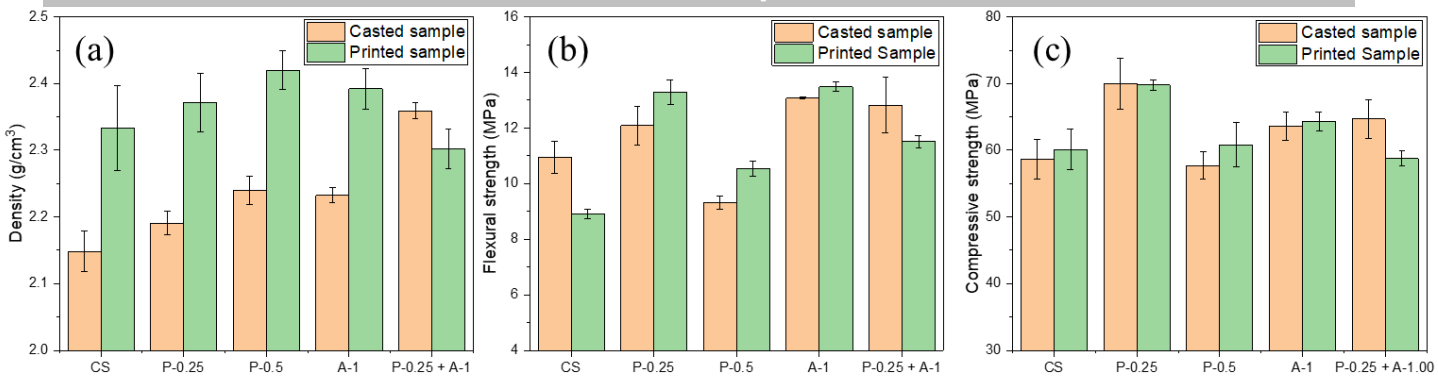

Figure 8 – Density and mechanical performance of casted and printed alkali-activated composites (a) density, (b) flexural strength, and (c) compressive strength at 7 days

Before the mechanical property tests, the samples' density, both printed and conventionally casted, were measured (shown in **Figure 8a)**. For samples with PVA fibres, the density of conventionally casted samples increased from 2.19 g/cm^3 for P-0.25 to 2.24 g/cm^3 for P-0.5, which are higher than the value registered for casted CS (i.e. 2.14 g/cm^3). On the other hand, the density of the printed samples also gradually increased from 2.33 g/cm^3 for CS to 2.37 g/cm^3 and 2.42 g/cm^3 for P-0.25 and P-0.5, respectively. The gradual densification by increasing the fibre content, both for printed and casted samples, is attributed to the adequate compatibility between the fibres and matrices. Further to this, a slightly higher density value was obtained for printed samples when comparing to the corresponding casted samples. This provides a confirmation that adequate compaction and integration of each extruded layer occurs during the extrusion process. Hence, the 3D printing process has the potential of minimising the formation of voids, which could be detrimental to the mechanical properties of the samples.

The incorporation of Attapulgite (i.e. A-1) caused a slight increase of 4% and 3% in density of casted and printed samples, respectively, compared to that of CS. The results are aligned with the results obtained from other studies [46], which provides further evidence that the addition of nano-clay leads to an increase in the density of alkali-activated mix. This suggests that the enhanced density recorded for the A-1 mix was attributed to the effective dispersion of these particles resulting in a less porous mix. For the hybrid sample (i.e. P-0.25+A-1) unexpected results were obtained, where the density of the casted sample was slightly higher (about 2.5%) than the printed one. This has to be associated with the high yield stress of the aforementioned mix, among the printable mixes, in the fresh state (see section 3.1), which led to inconsistent printing. This phenomenon generates trapped air babbles within the samples that reduces the density of printed sample compared to casted one.

The mechanical property results (**Figure 8b,c**) revealed that for all the mixes, except CS and P-0.25+A-1 samples, the flexural strength of the 3D printed parts are relatively higher compared to the casted counterparts. However, the compressive strength of all the printed samples show a comparable values to that of conventionally casted specimens, although a slight reduction in compressive strength was observed for the printed P-0.25+A-1 mix compared to the casted mix. In general, the incorporation of PVA fibers resulted in improved flexural and compressive strength of the printed samples. The flexural and compressive strength of P-0.25 was increased by 49%

and 16%, respectively, to that of the printed control sample. However, the incorporation of more PVA fibres (i.e. P-0.5) was shown to be less effective as the flexural and compressive strength increased by 18% and 1% compared to the printed control sample.

The enhanced flexural and compressive strength is attributed to three major mechanisms. First, the improved integration of the fibres within the alkali-activated matrices is reinforced by the extrusion process [47]. **Figure 9** indicates that the fibre was well embedded in the matrices as large amounts of activation products are observed on the fibre surface [48]. This is further supported by the use of EDS, which identified similar elements of the matrix presented on the fibre surface. As reported by Xu et al. (2017), PVA fibres react with alkali-activated composites, a transitional layer composed of activation products are produced at the interface between fibre and matrices, which make strong interfacial bonding between the matrices and fibres. Hence, PVA fibres can be more effectively distributed and connected within the cementitious paste [49]. The second mechanisms are the crack-bridging and crack blocking phenomena induced by the incorporation of fibres. As shown in **Figure 10**, after the micro-cracks initiation, the micro-cracks tend to propagate within the cementitious paste to form macro-cracks. However, PVA fibres that have crossed the crack and are anchored in the matrices on both sides, effectively 'sewing' the two sides together and preventing the crack from widening [50]. This results in increased flexural strength of the fiber-reinforced samples compared to both printed and casted CS. The third mechanism is the fibre alignment generated during the extrusion process within the alkali-activated paste [12,51]. In this hypothesis, during the extrusion process, the nozzle enables fibre alignment along the printing path, which can lead to an increase in flexural strength of the printed structures in a perpendicular load direction [52]. Several studies have demonstrated the feasibility of developing a 3D-printable fibre-reinforced cementitious composite and reported the positive impact of fibre alignment on the samples' mechanical performance [53–55].

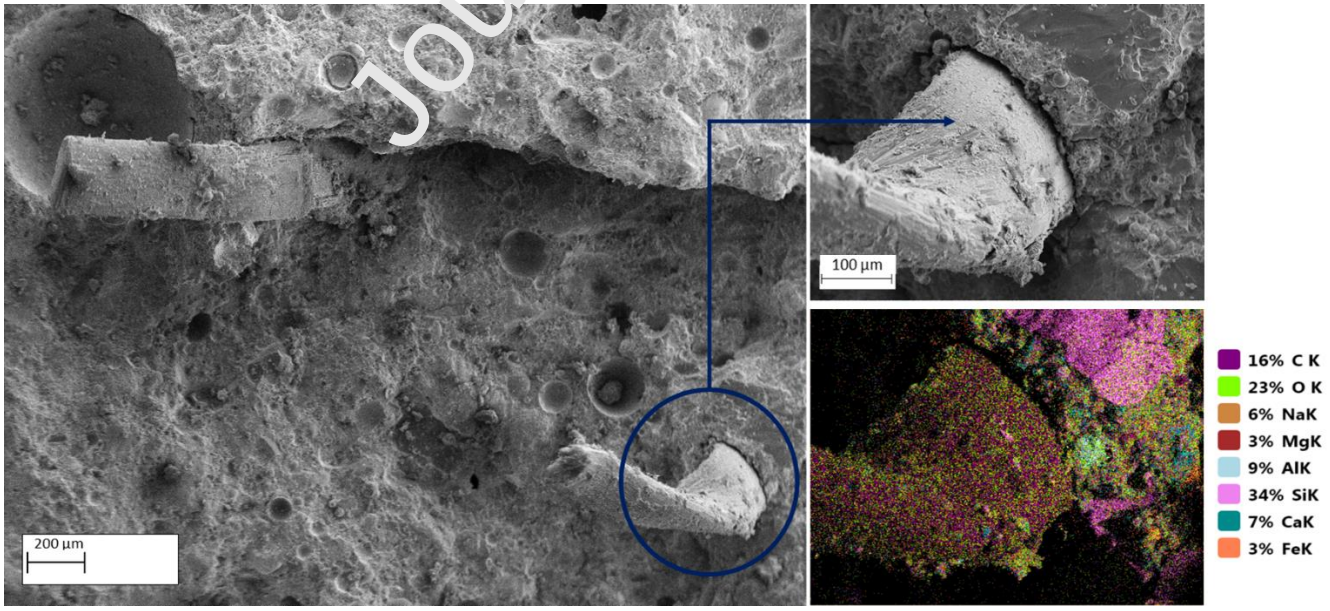

Figure 9 – Microstructure analysis (SEM/EDS) of 3D printed PVA-reinforced alkali-activated composite

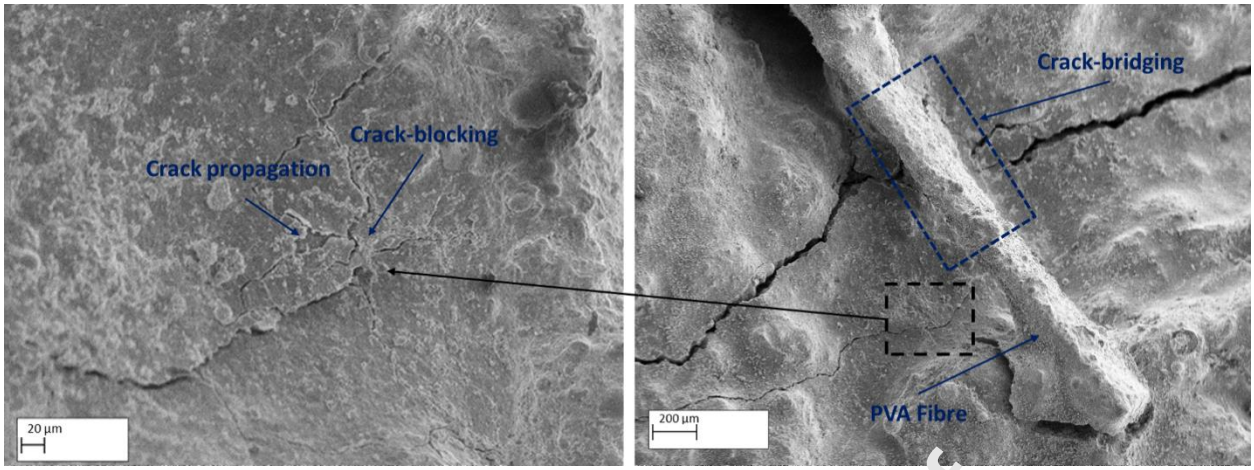

Figure 10 – Microstructure analysis of 3D printed samples reinforced with PVA fibres in the fracture zone

The nano-clay additive, on the other hand, similarly increased the mechanical strength of the material. The addition of 1% attapulgite nano-clay (i.e. A-1) led to an increase in flexural and compressive strength from 9 MPa and 60 MPa for printed CS to 13.5 MPa and 64 MPa for A-1 printed samples, respectively (see **Figure 8b,c**). This could be attributed to the induced thixotropic behaviour of a mix through the addition of nano-clay generated by the rapture of the inter-particle links within the matrix under the shear-force of the extrusion process. After the printing process, due to the reversible behaviour of the thixotropic effect, the inter-particle links are rebuilt more robustly than before, resulting in the increased mechanical performance of the alkali-activated composite [16,25]. Another possible explanation, as demonstrated in **Figure 11b**, is that nano-clay incorporation accelerates the alkali-reaction process, leading to a higher amount of activation products and lower unreacted fly ash particles [46,56,57]. Moreover, the effective dispersion of nano-clay particles within the cementitious matrices leads to an improved porosity structure (see **Table 5**), thus, producing a more compact matrix structure compared to that of CS (**see Figure 11a**). Assaedi et al. (2016), also reported that the addition of up to 2% Cloisite 30B nano-clay particles to a geopolymer mix induced a remarkable increase in both flexural and compressive strength [46]. For P-0.25+A-1 sample, the flexural strength was increased by 29% however the compressive strength slightly decreased (i.e. 2%) compared to that of printed CS. As can be seen in **Figure 8b and c**, both flexural and compressive strength of P-0.25+A-1 are relatively lower than the values registered for individual A-1 and P-0.25. This is attributed to their respective poor fresh properties as previously discussed. The microstructure analysis further proved that the adhesion between the fibers and matrices decreased due to the lower workability of the mixture in a fresh state. As it is evident in **Figure 11c and d**, some unreacted fly ash and nano-clay particles are present between the fiber and matrices interface, which increases the stress concentration, hence decreasing mechanical performance.

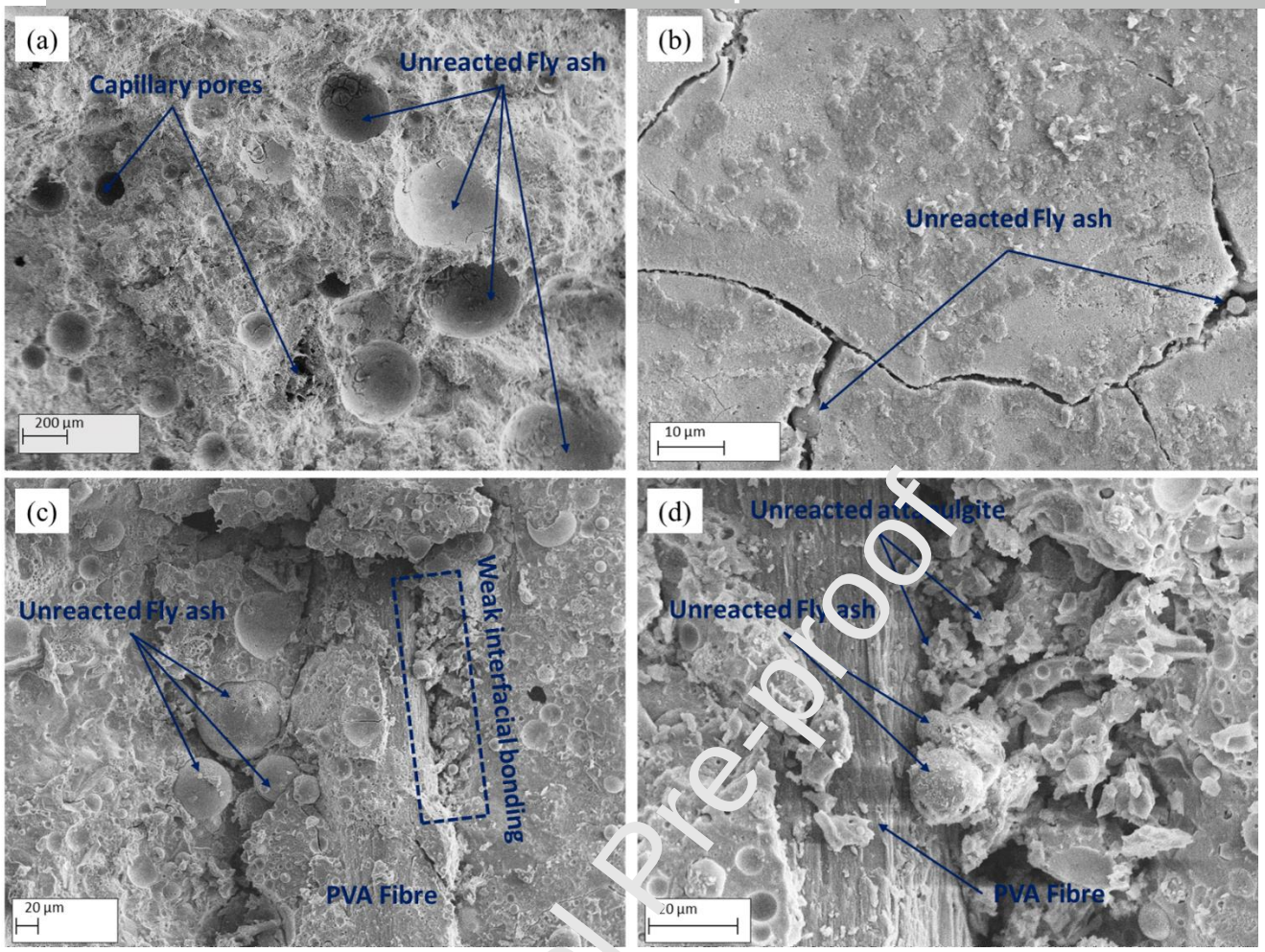

Figure 11 – Microstructural analysis of the fracture zone of 3D printed (a) Control sample X100, (b) A-1 X3K, (c) and (d) P-0.25+A-1

3.3 Effect of additives incorporation on 2D and 3D structure

Table 4 and **Figure 12** present the details of the Rapid Air void measurements obtained from vertical cross sections of printed specimens except P-0.5 that is eliminated due to poor mechanical performance compared to CS. Evaluation of the chord length frequency (**Figure 12**) confirms that specimens mostly consists fine voids. However, a significant difference between chord length frequency curves can be distinguished between the control sample (CS) and modified specimens. CS specimen exhibit significantly broader void distribution with higher contribution of coarser pores, while modified specimens possess higher quantity of fine voids. The contribution of so-called micro air voids (<300 microns) to the total air content of specimens CS, P-0.25, A-1 and P-0.25+A-1 is 53 %, 80 %, 83 % and 70 %, respectively. The total air content of specimens is relatively comparable, however, the lowest air content was reported for specimen 0.25-PVA which is 11 % lower when compared to CS specimen. The refinement of the void structures in specimens is also confirmed by other parameters such as average chord length and spacing factor, which confirms the decrement of the average void size as well as overall refinement of the void structure. This could be responsible for the observed strength improvements in modified specimens (**Figure 8**).

Table 4 – 2D void characteristics properties of specimens cross-sections obtained with RapidAir device

Air void Parameter	CS	P-0.25	A-1	P-0.25+A-1
Air content [%]	3.54	3.16	3.54	3.32
Average chord length [mm]	0.158	0.087	0.081	0.082
Specific surface [mm^{-1}]	25.38	46.13	49.33	49.03
Spacing factor [mm]	0.2319	0.1343	0.1193	0.1236

Rapid Air technique can provide a good insight into general (averaged) void pore structure, however, does not enable the evaluation of the volumetric voids characteristics. Moreover, the alteration of the microstructure along the height of specimen cannot be determined. Therefore, micro-CT technique was adapted towards understanding the void characteristics along the height of specimen.

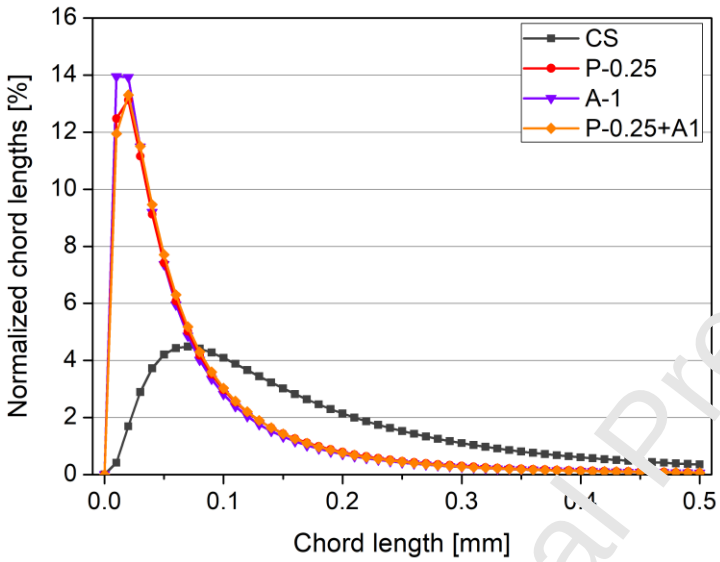

Figure 12 – Chord length-frequency distribution in 3D printed specimens

In each additive case, three different positions were selected at the top, middle, and bottom part of the specimens, and a total of 12 cases were investigated (**Figure 3**). Since the main target of the micro-CT measurement is the pore characteristics, the pore structure of each specimen was visualized as shown in **Figure 13**. In this figure, the gray part denotes the pores inside the specimens, and it can be confirmed that the pores within the specimens show directional dependency, although the degree of anisotropy varies according to the positions and additive types. Porosities of specimens measured on different height of specimen exhibits variation and in generally higher quantities of voids can be reported in lower and middle sections of specimens (**Table 5**). However, on average the total porosities from 3 tested heights are comparable to that of total air content value determined with RapidAir (**Table 4**). The slight discrepancy between the results is attributed to the different measuring ranges of both techniques.

For qualitative and quantitative investigation, the lineal-path function (L_2) was adopted in this study. **Figure 14** shows the results of the L_2 function for the cases in **Figure 13**. As can be seen in the figures, all cases show anisotropic characteristics in their pore structures. This indicates that the pores within the specimens are anisotropic, particularly

in the relatively large pores. In addition to the pore anisotropy, the porosity in each specimen at different locations can be found from the function at r/D is equal to zero.

For a quantitative investigation, the L_2 functions were integrated over the r/D, and the area in each function was computed. **Table 5** shows the quantitative results of the L_2 function and the porosity in each case. In this table, the integrated value denotes the degree of pore size along the direction, and the directional difference between the values in each specimen represents the degree of pore anisotropy (anisotropy ratio). The higher anisotropy ratio indicates that the specimen at that location contains more anisotropic pores, which can affect the stability of printed samples. Specimens CS and the P-0.25+A-1 show the highest anisotropic indexes, which indicate instability of the pores (**Figure 14**). Among the studied samples, the A-1 specimen shows the most stable and small anisotropy ratio that guarantees the quality of the printed material. These observations are in line with the results from the effect of additive incorporation on fresh properties and buildability investigations. The A-1 sample has satisfactory shape retention characteristics as well as the best buildability among the tested specimens, which will be discussed in the next section. It can be concluded that A-1 is the most homogenous mixture over the height between all the investigated samples. The lowest pores anisotropy as well as overall refinement of the microstructure in A-1 can also be correlated with the best mechanical performance.

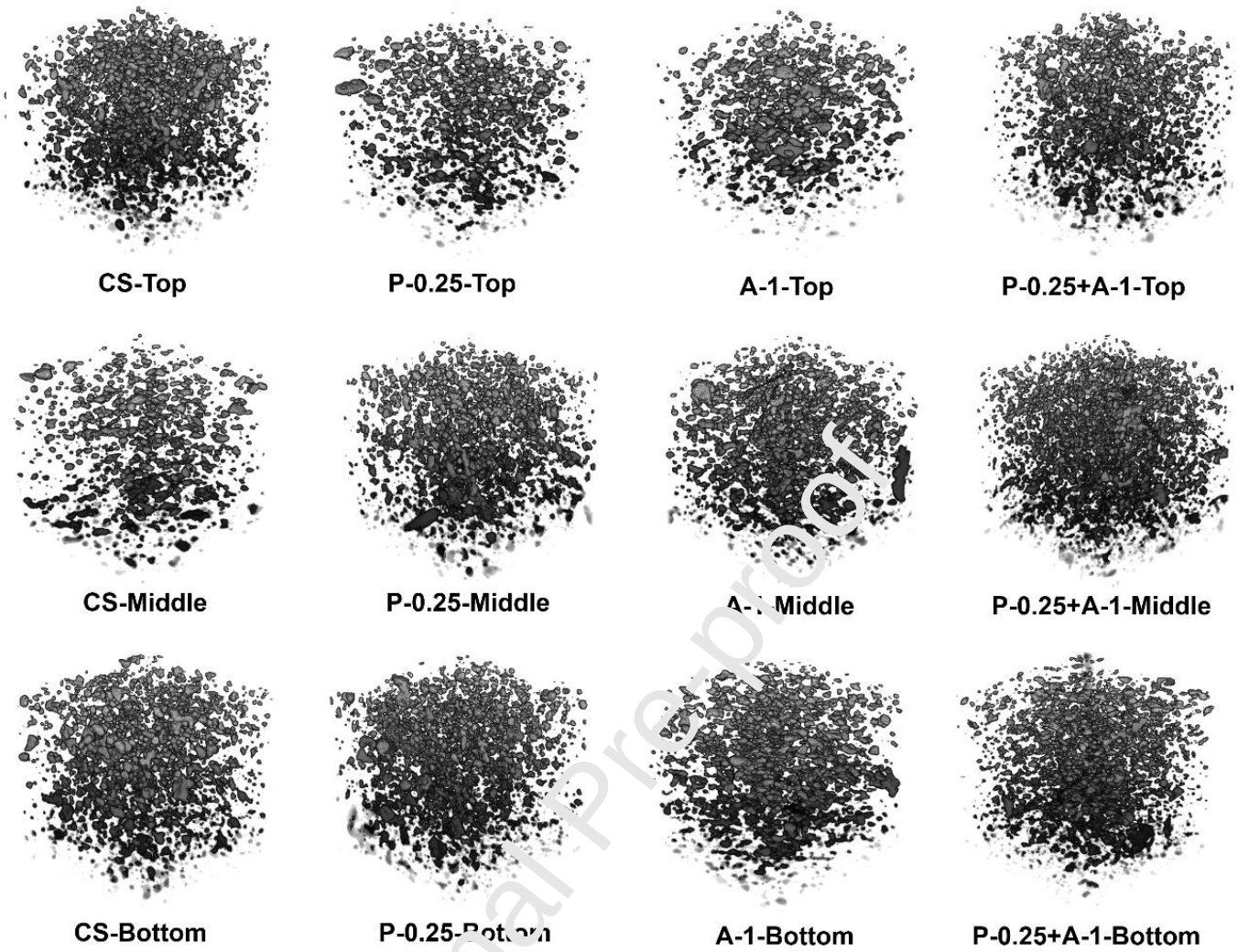

Figure 13 – Pore structures of the measured specimens (Note: the gray region represents pores inside each specimen.)

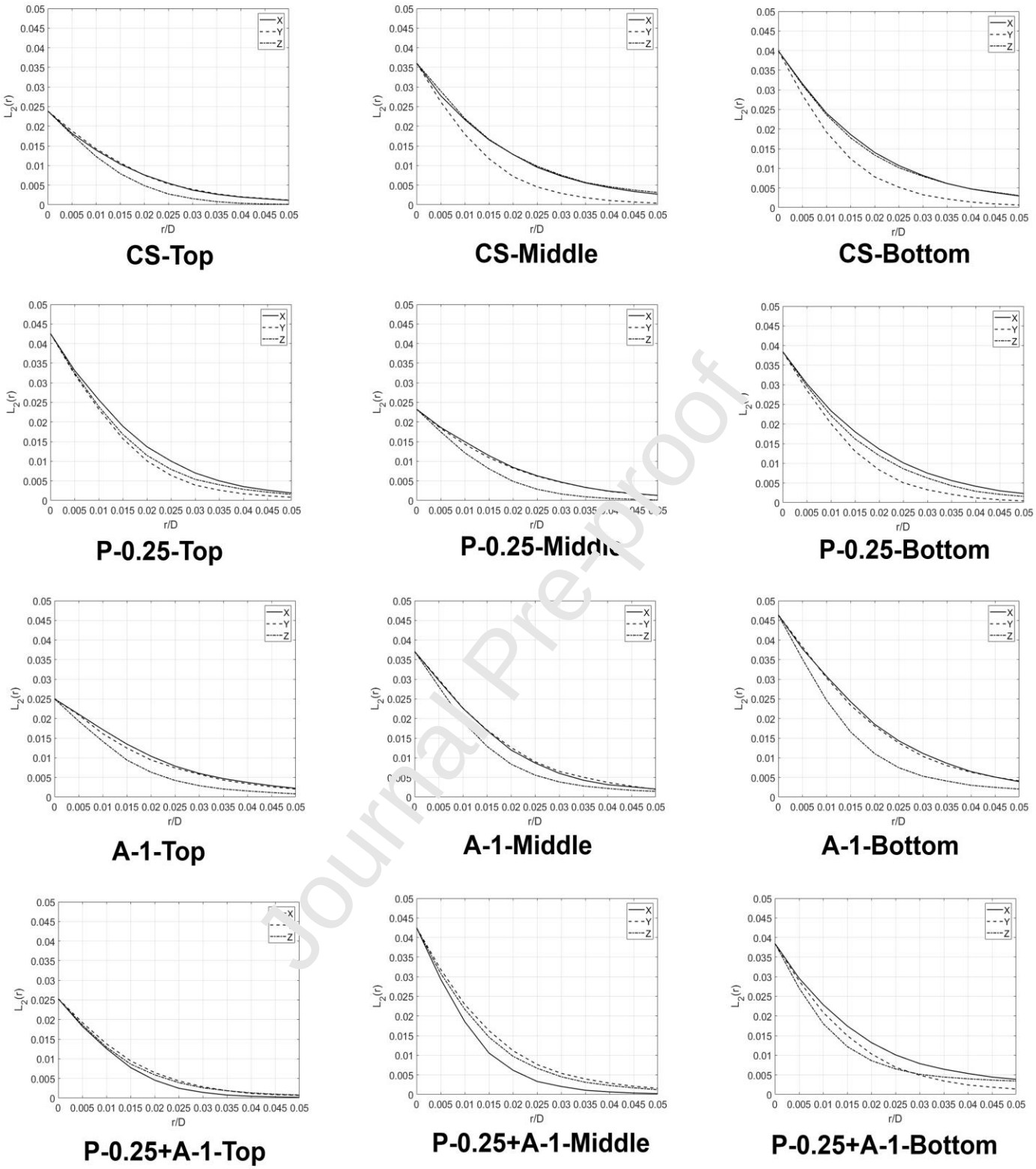

Figure 14 – Lineal-path function for the measured specimens at different locations (Note: in each graph, the *x*-axis denotes the relative length of the test line, while the *y*-axis denotes function value.)

Table 5 – Pore characteristics obtained from micro-CT and integration of the L_2 function in each direction and location

Specimen	Location	L_2 integration			Anisotropy ratio [max/min]	Porosity [%]	Average porosity [%]
		X	Y	Z			
CS	**Top**	4.38E-04	4.30E-04	3.04E-04	1.441675	2.39	3.34
	Middle	7.43E-04	4.60E-04	7.42E-04	1.614963	3.61	
	Bottom	8.12E-04	5.35E-04	7.82E-04	1.517664	4.01	
P-0.25	**Top**	7.64E-04	6.12E-04	6.98E-04	1.249056	4.26	3.48
	Middle	4.66E-04	4.80E-04	2.93E-04	1.637086	2.33	
	Bottom	7.34E-04	5.08E-04	6.64E-04	1.444532	3.84	
A-1	**Top**	5.19E-04	4.81E-04	3.94E-04	1.31889	2.5	3.62
	Middle	6.83E-04	6.60E-04	6.00E-04	1.138456	3.71	
	Bottom	9.56E-04	9.95E-04	7.62E-04	1.306551	4.64	
P-0.25+A-1	**Top**	2.96E-04	3.62E-04	3.58E-04	1.223706	2.53	3.54
	Middle	4.75E-04	6.74E-04	6.15E-04	1.420767	4.25	
	Bottom	8.25E-04	6.37E-04	0.0013	2.141645	3.85	

3.4 Buildability test

The buildability performance of each printable mix, selected in previous section (i.e. section 3.3), is displayed in **Figure 15a-d**. The qualitative results indicated that all mixtures were printed without considerable radial distortion and adequate surface finish. However, due to the higher yield shear stress and low flowability of the fresh mixture, the printed cylinder's outer surface with PVA and attapulgite nano-clay (i.e. P-0.25+A-1) showed visible segregations. Moreover, due to the compressive load induced by the deposition of top layers, the reduction in bottom layers height was clearly observed for all mixtures. The maximum printing height of each object after printing was also measured. The results indicated that by printing the constant quantity of fresh materials (i.e. 5500 g), the incorporation of additives led to an increase in the maximum height of printed cylinders from 117 mm for the control sample (see **Figure 15a**) to 125 mm (see **Figure 15b**), 120 mm (see **Figure 15c**) and 138 mm (see **Figure 15d**) for A-1, P-0.25, and P-0.25+A-1 samples, respectively. As it can be seen in **Table 3**, the results are fully aligned with the rheology results as yield shear stress also showed that control sample had lower yield shear stress (i.e. 1215.62 Pa.s) compared to that of A-1 (i.e. 1797.11 Pa.s), P-0.25 (i.e. 1361.18 Pa.s), and P-0.25+A-1 (i.e. 1889.6 Pa.s). Direct relation between the

rheology parameters and buildability of printed objects proves the capability of rheology measurements as a practical tool for both mix selection and prediction of materials buildability before the printing process.

Figure 15 – Buildability of the printed samples, (a) control sample, (b) P-0.25, (c) A-1, and (d) P-0.25+A-1.

4. Conclusions

The main objective of this study was to investigate the impact of two additives (i.e. PVA fibres and attapulgite nano-clay) on the fresh properties of alkali-activated materials in terms of flowability, rheology, mini slump, extrusion window, and shape retention. Further, the printed samples' mechanical properties (i.e. density, flexural and compressive strength) were evaluated and compared to the corresponding casted samples. Finally, the reinforcing mechanisms of additives were elucidated by the correlations between the fresh properties, buildability, and mechanical properties as well as the 2D and 3D microstructure analysis (i.e. SEM, RapidAir measurement, and µ-CT scan) of the specimens. The following conclusive statement can be drawn from this study:

- The incorporation of both attapulgite and PVA fibres in specific dosages can lead to improvements in the fresh properties of alkali-activated mix. Both additives at specific dosages induce an adequate decrease in

flow ability, slump height along with a sufficient increase in shape retention, yield shear stress, and extrusion window.

- Amongst the investigate AAM mixes, P-0.25, A-1, and P-0.25+A-1 meet the basic buildability requirements needed for 3D printing. The inclusion of additives slightly increased the maximum height of printed objects compared to the control sample.
- P-0.25 and A-1 were found to be the best performing sample in terms of 3D printing and mechanical performance. For P-0.25, the flexural and compressive strength increased by 24% and 10 %, respectively, compared to the printed control sample. Samples with 1% attapulgite (i.e. A-1) also experienced increased flexural and compressive strength by 43% and 20%, respectively, compared to the printed control sample. This increase in mechanical performance is most likely attributed to good dispersion of nano-clay particles and fibers crack-bridging mechanisms throughout the composite.
- The microstructure analysis clearly showed the effectiveness of attapulgite and PVA fibres incorporation in filling the voids and crack bridging mechanisms.
- The study found that both RapidAir and micro-CT techniques can be successfully used as complimentary measuring approaches towards understanding the microstructural characteristics of the 3D printed elements. Noticeable pores anisotropy has been over the height in selected specimens, however, appropriate mixture design helps to overcome this obstacle.
- The incorporation of 1 wt.-% attapulgite clay exhibits the most satisfactory microstructural characteristics with the lowest pores anisotropy as well as mixture homogeneity. This results in the best mechanical performance and shape retention followed by buildability.

The promising breakthroughs of this study on the positive impacts of fibre and nano-clay additives in 3D printing of alkali-activated materials can lead to potential applications for large-scale construction. Future studies need focus on a more comprehensive mix design formulations to yield conclusive outcomes with statistical analysis and verification. Moreover, the reaction mechanisms and functionalities of the additives in determination of various properties of 3D printed AAMs should be elaborated.

Acknowledgements

Pawel Sikora received funding from the European Union's Horizon 2020 research and innovation program under the Marie Skłodowska-Curie grant agreement no. 841592.

Conflict of interest : None

References

[1] M. Xia, J. Sanjayan, Method of formulating geopolymer for 3D printing for construction applications, JMADE.

110 (2016) 382–390. doi:10.1016/j.matdes.2016.07.136.

[2] B. Nematollahi, M. Xia, P. Vijay, J.G. Sanjayan, Properties of Extrusion-Based 3D Printable Geopolymers for Digital Construction Applications, Elsevier Inc., 2019. doi:10.1016/B978-0-12-815481-6.00018-X.

[3] B. Nematollahi, J. Sanjayan, F.U.A. Shaikh, Synthesis of heat and ambient cured one-part geopolymer mixes with different grades of sodium silicate, Ceram. Int. 41 (2015) 5696–5704. doi:10.1016/j.ceramint.2014.12.154.

[4] S. Hamidreza, J. Corker, M. Fan, Automation in Construction Additive manufacturing technology and its implementation in construction as an eco-innovative solution, 93 (2018) 1–11. doi:10.1016/j.autcon.2018.05.005.

[5] S. Ghaffar, P. Mullett, Commentary : 3D printing set to transform the construction industry, Struct. Build. (2018) 1–2. doi:https://doi.org/10.1680/jstbu.18.00136.

[6] P. Duxson, J.L. Provis, F. Si, Designing Precursors for Geopolymer Cements, 3869 (2008) 3864–3869. doi:10.1111/j.1551-2916.2008.02787.x.

[7] B. Panda, M.J. Tan, Experimental study on mix proportion and fresh properties of fly ash based geopolymer for 3D concrete printing, Ceram. Int. 44 (2018) 10258–10265. doi:10.1016/j.ceramint.2018.03.031.

[8] B. Panda, S.C. Paul, L.J. Hui, Y.W.D. Tay, M.J. Tan, Additive manufacturing of geopolymer for sustainable built environment, J. Clean. Prod. 167 (2018) 281–288. doi:10.1016/j.jclepro.2017.08.165.

[9] G.M. Rao, T.D.G. Rao, Final Setting Time and Compressive Strength of Fly Ash and GGBS-Based Geopolymer Paste and Mortar, (2015) 3067–3074. doi:10.1007/s13369-015-1757-z.

[10] H. Alghamdi, S.A.O. Nair, N. Neithalath, Insights into material design , extrusion rheology , and properties of 3D- printable alkali-activated fl y ash-based binders, Mater. Des. 167 (2019) 107634. doi:10.1016/j.matdes.2019.107634.

[11] B. Nematollahi, M. Xia, J. Sanjayan, P. Vijay, Effect of type of fiber on inter-layer bond and flexural strengths of extrusion-based 3D printed geopolymer, Mater. Sci. Forum. 939 (2018) 155–162. doi:10.4028/www.scientific.net/MSF.939.155.

[12] B. Zhu, J. Pan, B. Nematollahi, Z. Zhou, Y. Zhang, J. Sanjayan, Development of 3D printable engineered cementitious composites with ultra-high tensile ductility for digital construction, Mater. Des. 181 (2019) 108088. doi:10.1016/j.matdes.2019.108088.

[13] B. Panda, S. Ruan, C. Unluer, M.J. Tan, Investigation of the properties of alkali-activated slag mixes involving

the use of nanoclay and nucleation seeds for 3D printing, Compos. Part B Eng. 186 (2020). doi:10.1016/j.compositesb.2020.107826.

[14] M. Chougan, S. Hamidreza Ghaffar, M. Jahanzat, A. Albar, N. Mujaddedi, R. Swash, The influence of nano-additives in strengthening mechanical performance of 3D printed multi-binder geopolymer composites, Constr. Build. Mater. 250 (2020) 118928. doi:10.1016/j.conbuildmat.2020.118928.

[15] Y.W.D. Tay, Y. Qian, M.J. Tan, Printability region for 3D concrete printing using slump and slump flow test, Compos. Part B Eng. 174 (2019) 106968. doi:10.1016/j.compositesb.2019.106968.

[16] N. Roussel, G. Ovarlez, S. Garrault, C. Brumaud, The origins of thixotropy of fresh cement pastes, Cem. Concr. Res. 42 (2012) 148–157. doi:10.1016/j.cemconres.2011.09.004.

[17] N. Roussel, Rheological requirements for printable concretes, Cem. Concr. Res. 112 (2018) 76–85. doi:10.1016/j.cemconres.2018.04.005.

[18] B. Nematollahi, P. Vijay, J. Sanjayan, A. Nazari, M. Xia, V.N. Nerella, V. Mechtcherine, Effect of Polypropylene Fibre Addition on Properties of Geopolymers Made by 3D Printing for, (2018). doi:10.3390/ma11122352.

[19] B. Panda, S. Chandra Paul, M. Jen Tan, Anisotropic mechanical performance of 3D printed fiber reinforced sustainable construction material, Mater. Lett. 209 (2017) 146–149. doi:10.1016/j.matlet.2017.07.123.

[20] B. Panda, C. Unluer, M. Jen, Extrusion and rheology characterization of geopolymer nanocomposites used in 3D printing, Compos. Part B. 176 (2019) 107290. doi:10.1016/j.compositesb.2019.107290.

[21] A.C. De Leon, Q. Chen, N.B. Palaganas, J.O. Palaganas, J. Manapat, R.C. Advincula, High performance polymer nanocomposites for additive manufacturing applications, React. Funct. Polym. 103 (2016) 141–155. doi:10.1016/j.reactfunctpolym.2016.04.010.

[22] A. Albar, M. Chougan, M.J. Al- Kheetan, M.R. Swash, S.H. Ghaffar, Effective extrusion-based 3D printing system design for cementitious-based materials, Results Eng. 6 (2020) 100135. doi:10.1016/j.rineng.2020.100135.

[23] K.B. Bai Kamara, E. Ganjian, M. Khorami, The effect of quarry waste dust and reclaimed asphalt filler in hydraulically bound mixtures containing plasterboard gypsum and GGBS, J. Clean. Prod. 279 (2021) 123584. doi:10.1016/j.jclepro.2020.123584.

[24] T.T. Nguyen, C.I. Goodier, S.A. Austin, Factors affecting the slump and strength development of geopolymer concrete, Constr. Build. Mater. 261 (2020) 119945. doi:10.1016/j.conbuildmat.2020.119945.

[25] B. Panda, S. Ruan, C. Unluer, M. Jen, Improving the 3D printability of high volume fl y ash mixtures via the use of nano attapulgite clay, Compos. Part B. 165 (2019) 75–83. doi:10.1016/j.compositesb.2018.11.109.

[26] M. Tabatabaeian, A. Khaloo, A. Joshaghani, E. Hajibandeh, Experimental investigation on effects of hybrid fibers on rheological, mechanical, and durability properties of high-strength SCC, Constr. Build. Mater. 147 (2017) 497–509. doi:10.1016/j.conbuildmat.2017.04.181.

[27] A. Pierre, C. Lanos, P. Estellé, Extension of spread-slump formulae for yield stress evaluation, Appl. Rheol. 23 (2013). doi:10.3933/ApplRheol-23-63849.

[28] Z. Tan, S.A. Bernal, J.L. Provis, Reproducible mini-slump test procedure for measuring the yield stress of cementitious pastes, Mater. Struct. Constr. 50 (2017). doi:10.1617/s11527-017-1103-x.

[29] B.H. Mo, H. Zhu, X.M. Cui, Y. He, S.Y. Gong, Effect of curing temperature on geopolymerization of metakaolin-based geopolymers, Appl. Clay Sci. 99 (2014) 144–148. doi:10.1016/j.clay.2014.06.024.

[30] S.Y. Chung, P. Sikora, T. Rucinska, D. Stephan, M. Abd Elrahman, Comparison of the pore size distributions of concretes with different air-entraining admixture dosages using 2D and 3D imaging approaches, Mater. Charact. 162 (2020) 110182. doi:10.1016/j.matchar.2020.110182.

[31] N. Otsu, A Tlreshold Selection Method from Gray-Level Histograms, IEEE Trans. Syst. Man. Cybern. SM-C (1979) 62–66. doi:10.1109/TSMC.1979.4310076.

[32] A. Tewari, A.M. Gokhale, J.E. Spowart, D.B. Miracle, Quantitative characterization of spatial clustering in three-dimensional microstructures using two-point correlation functions, Acta Mater. 52 (2004) 307–319. doi:10.1016/j.actamat.2003.09.016.

[33] B. Lu, S. Torquato, Lineal-path function for random heterogeneous materials, Phys. Rev. A. 45 (1992) 922–929. doi:10.1103/PhysRevA.45.922.

[34] A.M. Gokhale, A. Tewari, H. Garmestani, Constraints on microstructural two-point correlation functions, Scr. Mater. 53 (2005) 989–993. doi:10.1016/j.scriptamat.2005.06.013.

[35] A. Favier, J. Hot, G. Habert, N. Roussel, J.B. D'Espinose De Lacaillerie, Flow properties of MK-based geopolymer pastes. A comparative study with standard Portland cement pastes, Soft Matter. 10 (2014) 1134–1141. doi:10.1039/c3sm51889b.

[36] M. Chougan, E. Marotta, F.R. Lamastra, F. Vivio, G. Montesperelli, U. Ianniruberto, A. Bianco, A systematic study on EN-998-2 premixed mortars modified with graphene-based materials, Constr. Build. Mater. 227 (2019) 116701. doi:10.1016/j.conbuildmat.2019.116701.

[37] M. Chougan, E. Marotta, F.R. Lamastra, F. Vivio, G. Montesperelli, U. Ianniruberto, S. Hamidreza, M.J. Al-kheetan, A. Bianco, High performance cementitious nanocomposites : The effectiveness of, Constr. Build.

Mater. 259 (2020) 119687. doi:10.1016/j.conbuildmat.2020.119687.

[38] N. Ranjbar, Z. Mingzhong, Fiber reinforced geopolymer composites: A review, Cem. Concr. Compos. 107 (2019). doi:https://doi.org/10.1016/j.cemconcomp.2019.103498.

[39] F. Liu, B. Wang, Y. Xing, K. Zhang, W. Jiang, Effect of polyvinyl alcohol on the rheological properties of cement mortar, Molecules. 25 (2020). doi:10.3390/molecules25030754.

[40] X. Zhou, Z. Li, Characterization of rheology of fresh fiber reinforced cementitious composites through ram extrusion, Mater. Struct. Constr. 38 (2005) 17–24. doi:10.1617/14064.

[41] C. Zhu, J. Zhang, J. Peng, W. Cao, J. Liu, Physical and mechanical properties of gypsum-based composites reinforced with PVA and PP fibers, Constr. Build. Mater. 163 (2018) 695–705. doi:10.1016/j.conbuildmat.2017.12.168.

[42] M. Cao, L. Li, New models for predicting workability and toughness of hybrid fiber reinforced cement-based composites, Constr. Build. Mater. 176 (2018) 618–628. doi:10.1016/j.conbuildmat.2018.05.075.

[43] R. Lediga, D. Kruger, Optimizing Concrete Mix Design for Application in 3D Printing Technology for the Construction Industry, 263 (2017) 24–29. doi:10.4028/www.scientific.net/SSP.263.24.

[44] T.T. Le, S.A. Austin, S. Lim, R.A. Buswell, A.G.F. Gibb, T. Thorpe, Mix design and fresh properties for high-performance printing concrete, Mater. Struct. Constr. 45 (2012) 1221–1232. doi:10.1617/s11527-012-9828-z.

[45] R.A. Buswell, W.R.L. De Silva, S.Z. Jones, J. Dirrenberger, Cement and Concrete Research 3D printing using concrete extrusion : A roadmap for research, Cem. Concr. Res. 112 (2018) 37–49. doi:10.1016/j.cemconres.2018.05.006.

[46] H. Assaedi, F.U.A. Shaikh, I.M. Low, Effect of nano-clay on mechanical and thermal properties of geopolymer, J. Asian Ceram. Soc. 4 (2016) 19–28. doi:10.1016/j.jascer.2015.10.004.

[47] Z. Pan, C. Wu, J. Liu, W. Wang, J. Liu, Study on mechanical properties of cost-effective polyvinyl alcohol engineered cementitious composites (PVA-ECC), Constr. Build. Mater. 78 (2015) 397–404. doi:10.1016/j.conbuildmat.2014.12.071.

[48] Y. Ling, P. Zhang, J. Wang, Y. Chen, Effect of PVA fiber on mechanical properties of cementitious composite with and without nano-SiO2, Constr. Build. Mater. 229 (2019). doi:10.1016/j.conbuildmat.2019.117068.

[49] F. Xu, X. Deng, C. Peng, J. Zhu, J. Chen, Mix design and flexural toughness of PVA fiber reinforced fly ash-geopolymer composites, Constr. Build. Mater. 150 (2017) 179–189. doi:10.1016/j.conbuildmat.2017.05.172.

[50] Q. Li, B. Huang, S. Xu, B. Zhou, R.C. Yu, Compressive fatigue damage and failure mechanism of fiber reinforced cementitious material with high ductility, Cem. Concr. Res. 90 (2016) 174–183. doi:10.1016/j.cemconres.2016.09.019.

[51] X. Qian, X. Zhou, B. Mu, Z. Li, Fiber alignment and property direction dependency of FRC extrudate, Cem. Concr. Res. 33 (2003) 1575–1581. doi:10.1016/S0008-8846(03)00108-X.

[52] G. Ma, Z. Li, L. Wang, F. Wang, J. Sanjayan, Mechanical anisotropy of aligned fiber reinforced composite for extrusion-based 3D printing, Constr. Build. Mater. 202 (2019) 770–783. doi:10.1016/j.conbuildmat.2019.01.008.

[53] D.G. Soltan, V.C. Li, A self-reinforced cementitious composite for building-scale 3D printing, Cem. Concr. Compos. 90 (2018) 1–13. doi:10.1016/j.cemconcomp.2018.03.017.

[54] S.C. Figueiredo, C.R. Rodríguez, Z.Y. Ahmed, E. Schlangen, F.P. Bos, Mechanical Behavior of Printed Strain Hardening Cementitious Composites, Materials (Basel). 13 (2020) 1–23. doi:https://doi.org/10.3390/ma13102253.

[55] A.R. Arunothayan, B. Nematollahi, R. Ranade, S.H. Bong, J. Sanjayan, Development of 3D-printable ultra-high performance fiber-reinforced concrete for digital construction, Constr. Build. Mater. 257 (2020) 119546. doi:10.1016/j.conbuildmat.2020.119546.

[56] H. Khater, Effect of Nano-Clay on Alkali Activated Water-Cooled Slag Geopolymer, Br. J. Appl. Sci. Technol. 3 (2013) 764–776. doi:10.9734/bjast/2014/2690.

[57] N.B. Singh, S.K. Saxena, M. Kumar, Effect of nanomaterials on the properties of geopolymer mortars and concrete, Mater. Today Proc. 5 (2018) 9035–9040. doi:10.1016/j.matpr.2017.10.018.

Graphical abstract

Highlights

- Poly-vinyl alcohol fibres and attapulgite nanoclay as additives for 3D printable alkali-activated materials
- P0.25 and A-1alkali-activated composites were found to be the best performing sample for 3D printability and mechanical performance
- The microstructure analysis showed the effectiveness of attapulgite and PVA fibres incorporation in filling the voids and crack bridging mechanisms

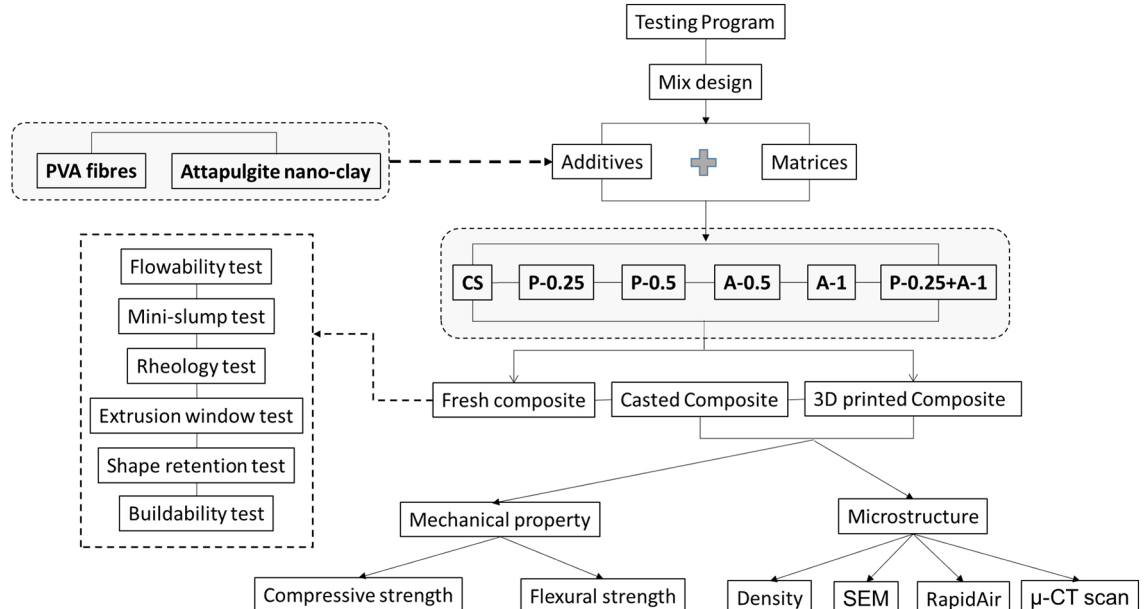

CS : Control sample; **P-0.25** : 0.25% PVA fibres; **P-0.5** : 0.5% PVA fibres; **A-0.5** : 0.5% Attapulgite nano-clay; **A-1** : 1% Attapulgite nano-clay; **P-0.25+A-1** : 0.25% PVA fibres +1% Attapulgite nano-clay

Figure 1

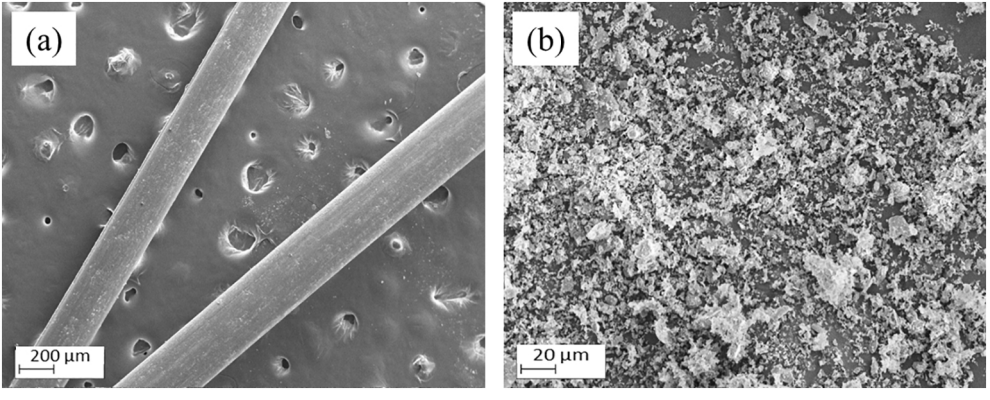

Figure 2

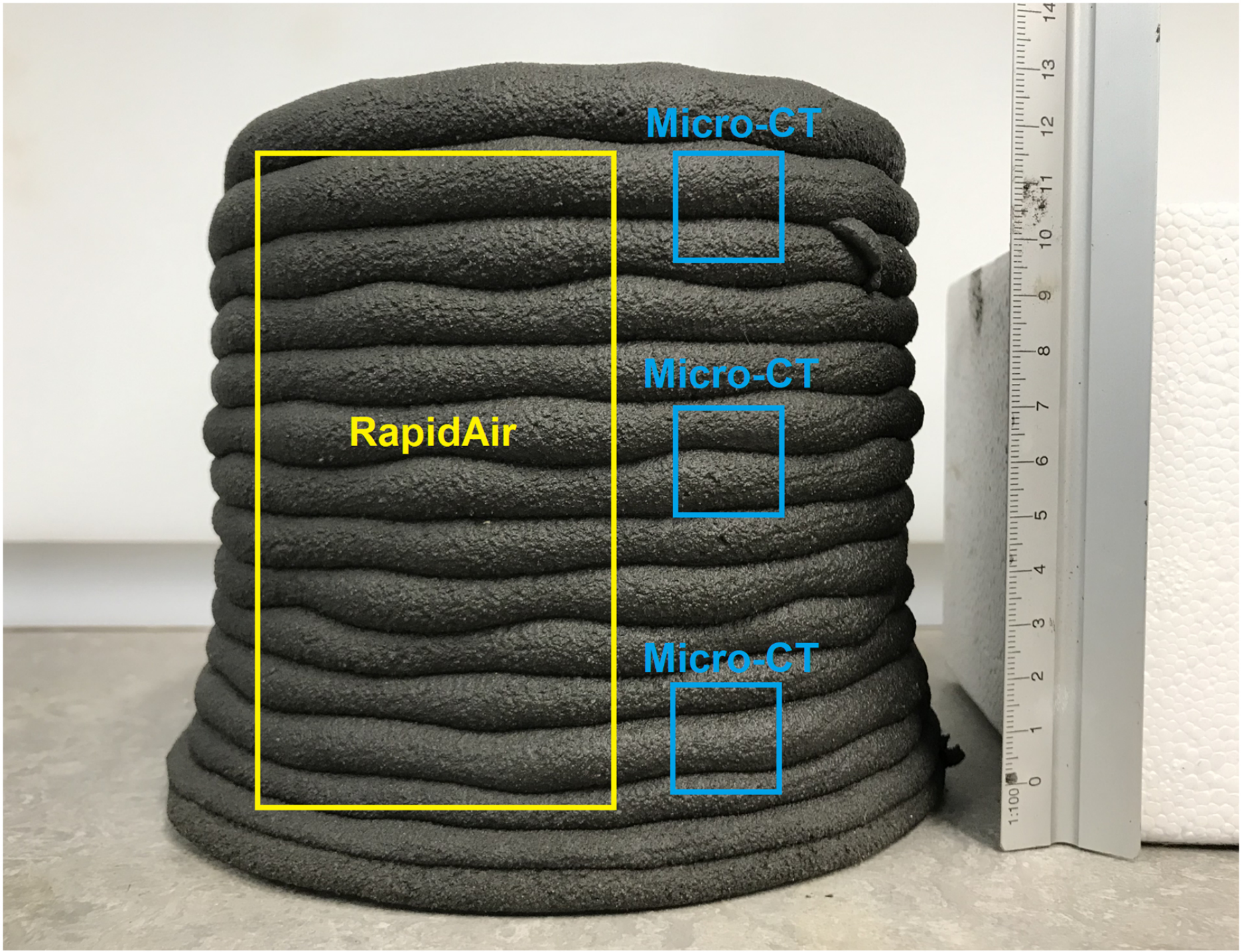

Figure 3

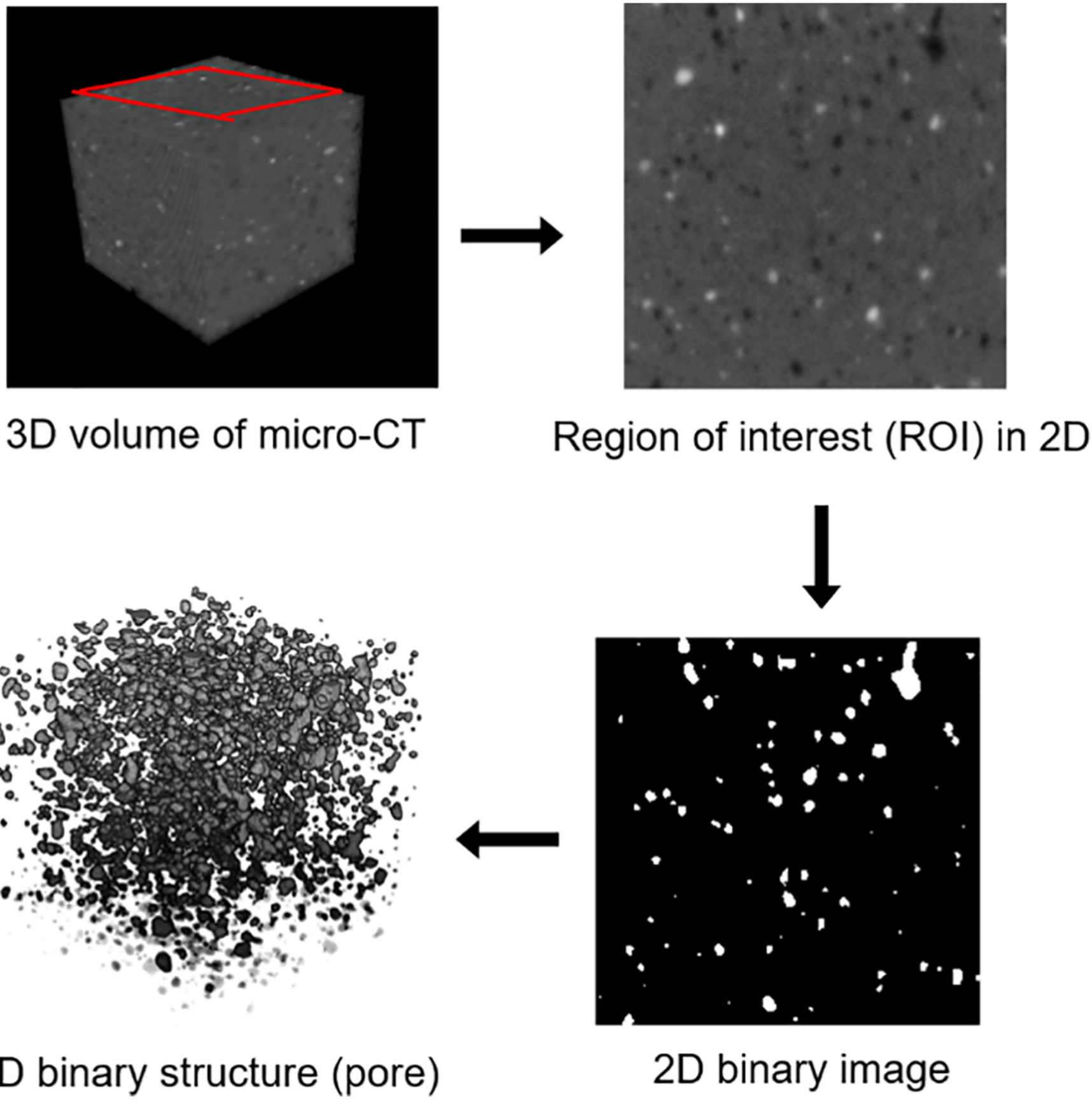
3D volume of micro-CT
Region of interest (ROI) in 2D
2D binary image
3D binary structure (pore)

Figure 4

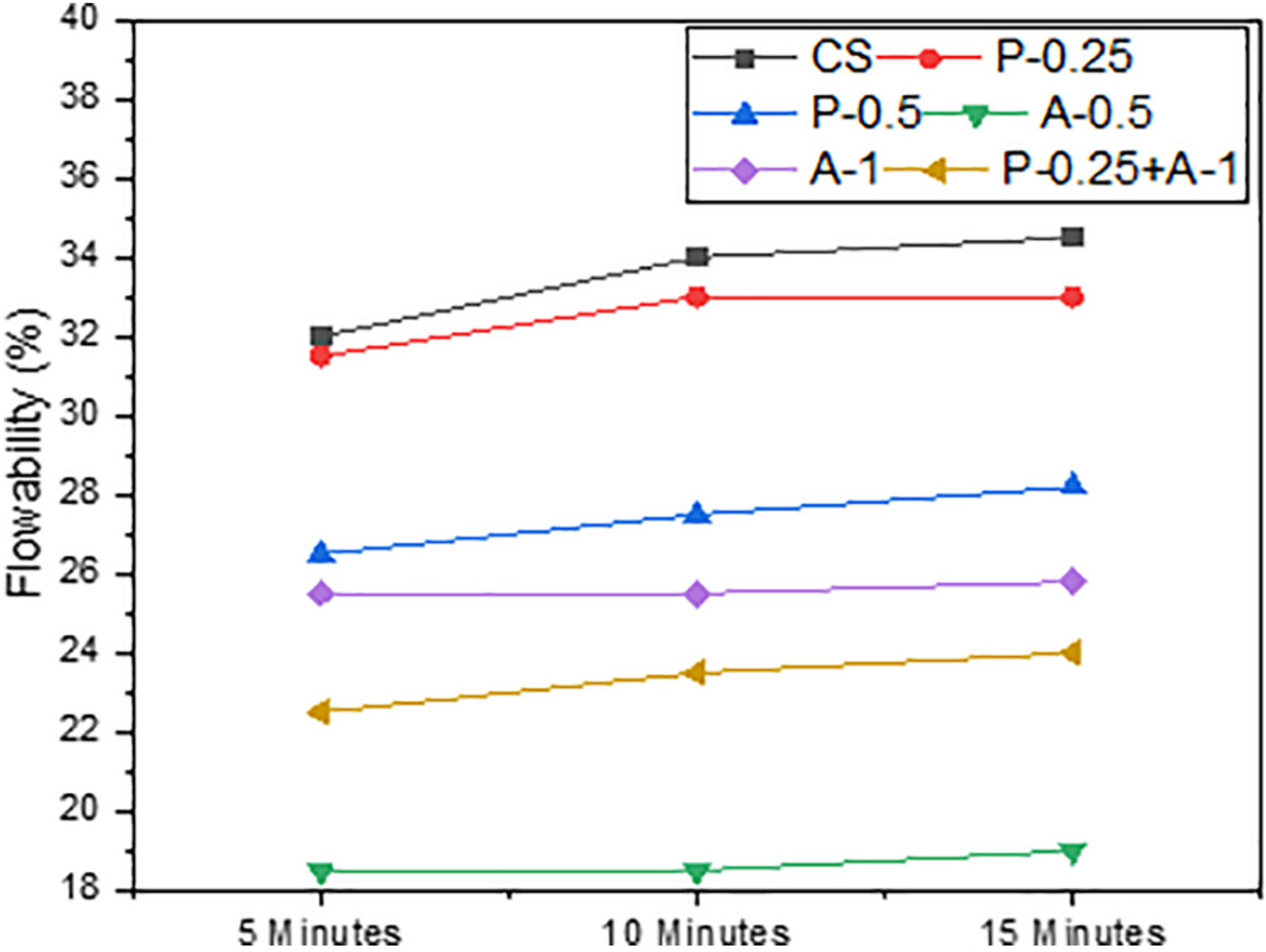
CS
P-0.25
P-0.5
A-0.5
A-1
P-0.25+A-1
Flowability (%)
40
38
36
34
32
30
28
26
24
22
20
18
5 Minutes
10 Minutes
15 Minutes

Figure 5

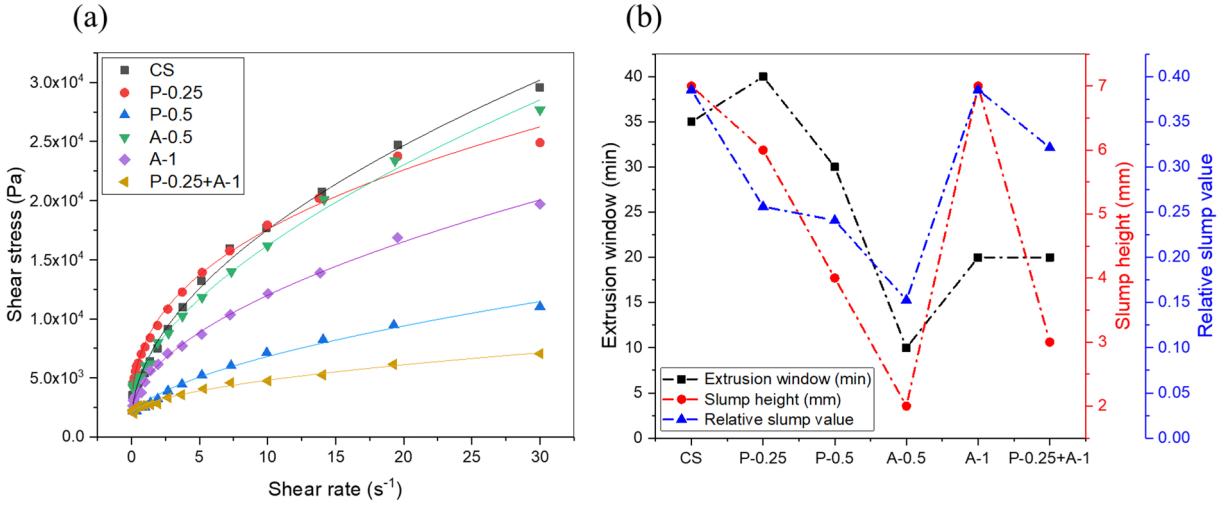
(a)
CS
P-0.25
P-0.5
A-0.5
A-1
P-0.25+A-1
Shear stress (Pa)
Shear rate (s-1)
(b)
Extrusion window (min)
Slump height (mm)
Relative slump value
CS
P-0.25
P-0.5
A-0.5
A-1
P-0.25+A-1

Figure 6

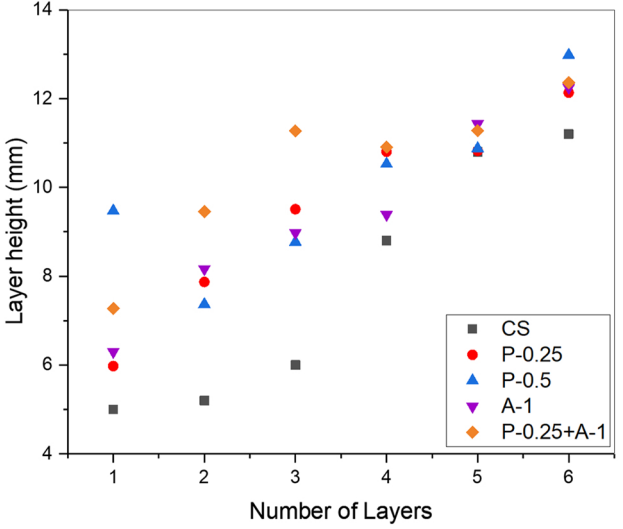
Layer height (mm)
Number of Layers
CS
P-0.25
P-0.5
A-1
P-0.25+A-1


(a)
20 mm


(b)
20 mm


(d)
20 mm


(c)
20 mm


(e)
20 mm

Figure 7

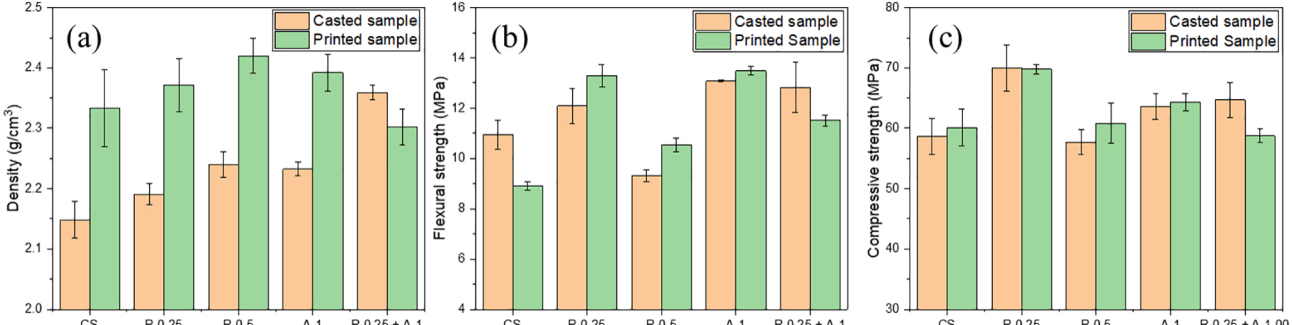
(a)
Casted sample
Printed sample
Density (g/cm3)
2.5
2.4
2.3
2.2
2.1
2.0
CS
P-0.25
P-0.5
A-1
P-0.25 + A-1
(b)
Casted sample
Printed Sample
Flexural strength (MPa)
16
14
12
10
8
6
4
CS
P-0.25
P-0.5
A-1
P-0.25 + A-1
(c)
Casted sample
Printed Sample
Compressive strength (MPa)
80
70
60
50
40
30
CS
P-0.25
P-0.5
A-1
P-0.25 + A-1.00

Figure 8

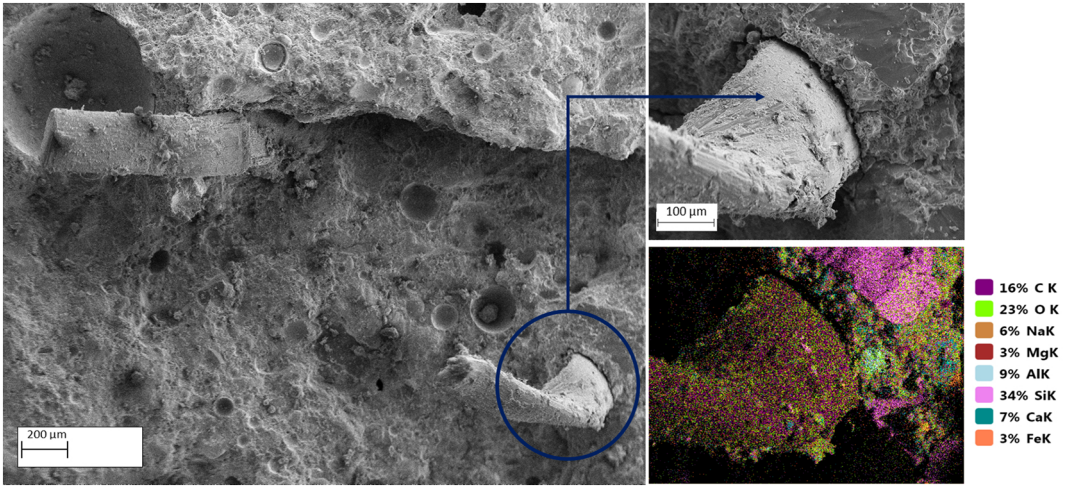

Figure 9

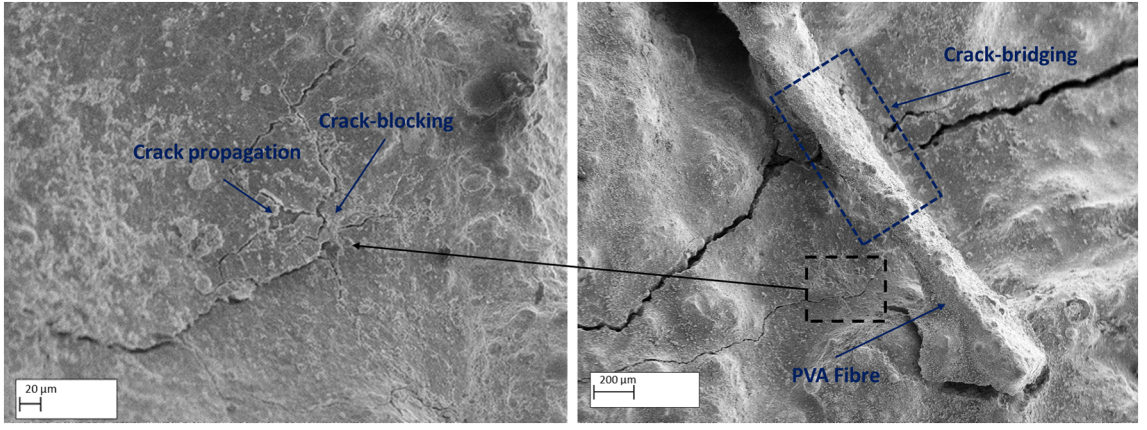
Crack propagation
Crack-blocking
20 µm
Crack-bridging
PVA Fibre
200 µm

Figure 10

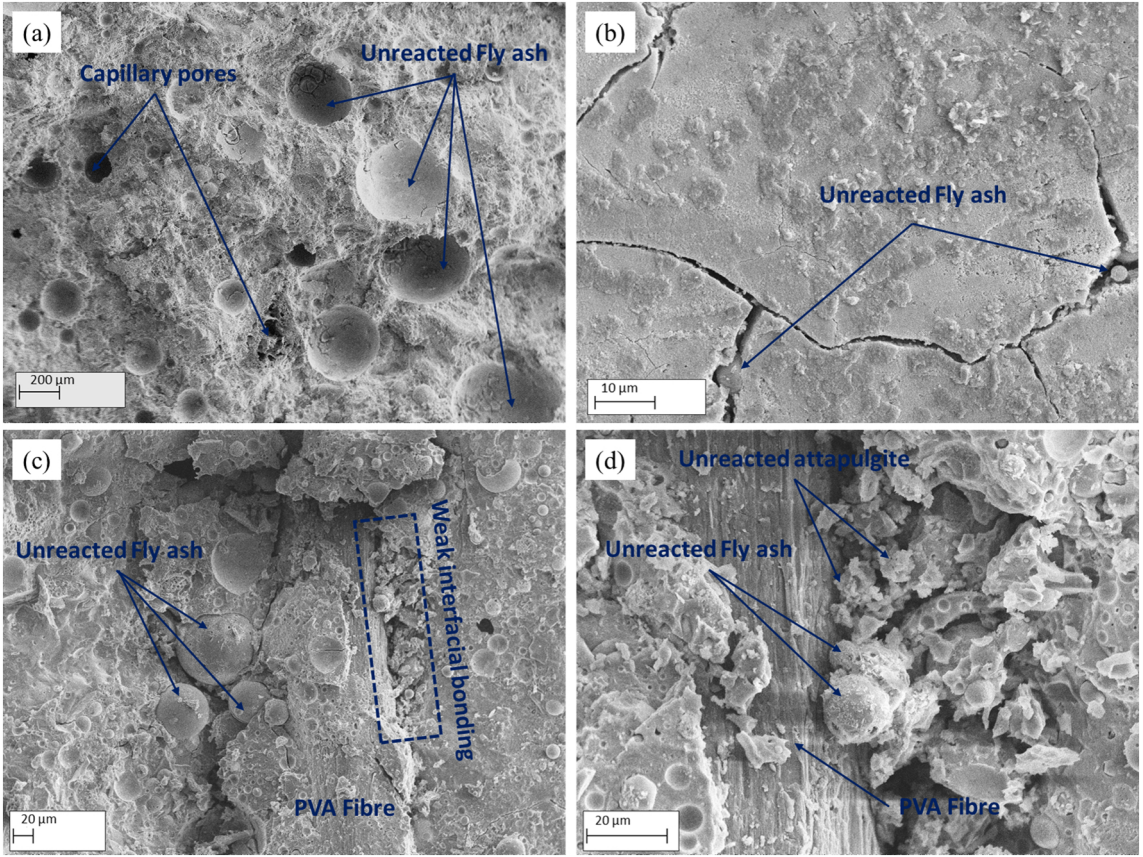
(a)
Capillary pores
Unreacted Fly ash
200 µm
(b)
Unreacted Fly ash
10 µm
(c)
Unreacted Fly ash
Weak interfacial bonding
PVA Fibre
20 µm
(d)
Unreacted attapulgite
Unreacted Fly ash
PVA Fibre
20 µm

Figure 11

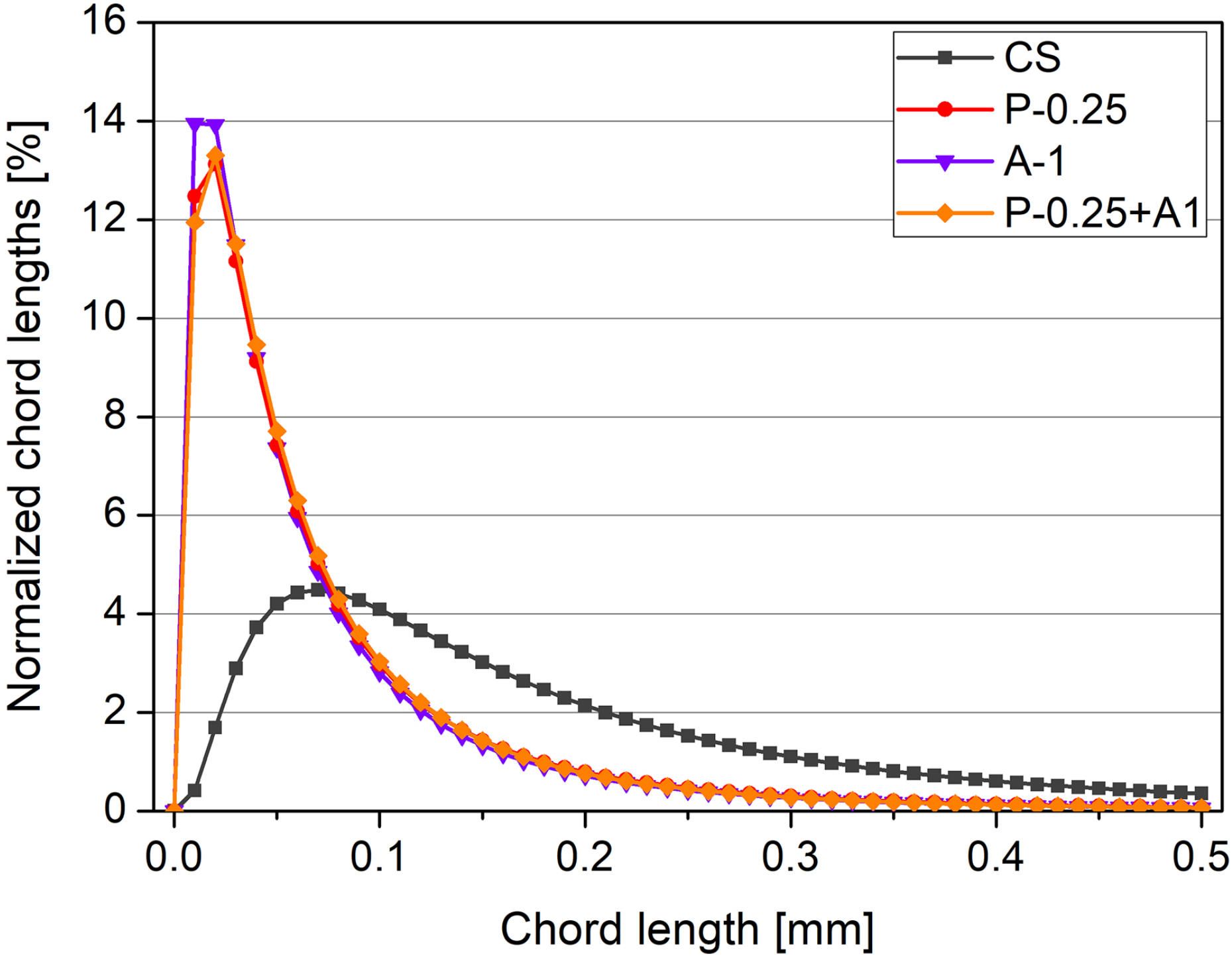
CS
P-0.25
A-1
P-0.25+A1
Normalized chord lengths [%]
Chord length [mm]
0
2
4
6
8
10
12
14
16
0.0
0.1
0.2
0.3
0.4
0.5

Figure 12

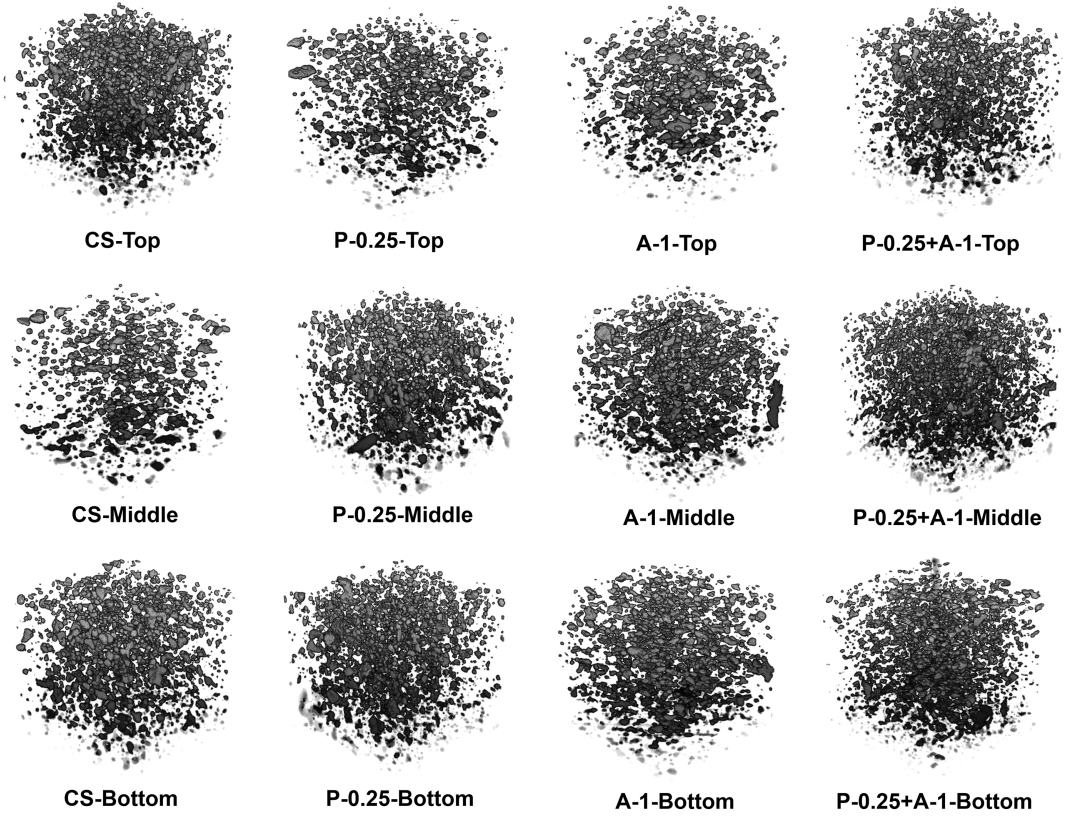
CS-Top
P-0.25-Top
A-1-Top
P-0.25+A-1-Top
CS-Middle
P-0.25-Middle
A-1-Middle
P-0.25+A-1-Middle
CS-Bottom
P-0.25-Bottom
A-1-Bottom
P-0.25+A-1-Bottom

Figure 13

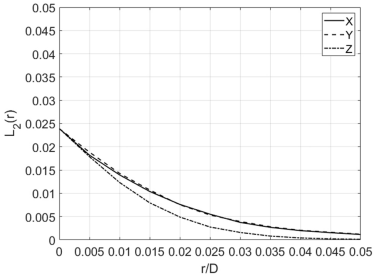

CS-Top

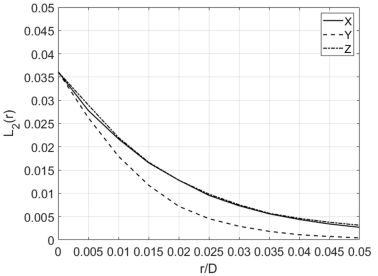

CS-Middle

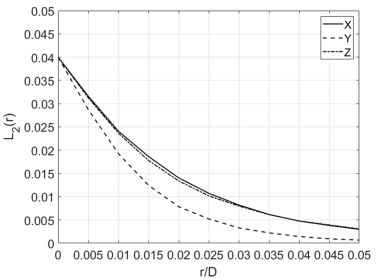

CS-Bottom

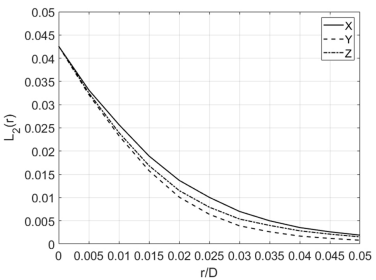

P-0.25-Top

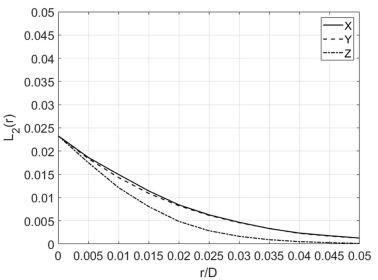

P-0.25-Middle

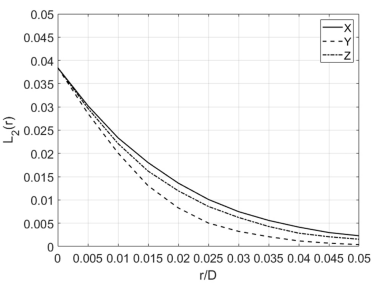

P-0.25-Bottom

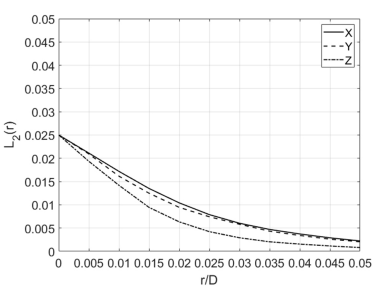

A-1-Top

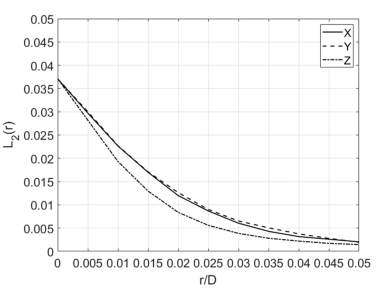

A-1-Middle

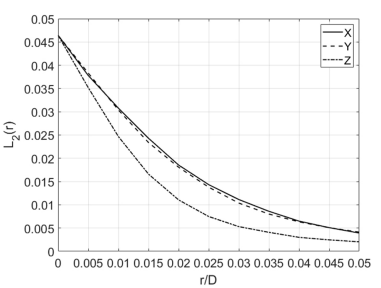

A-1-Bottom

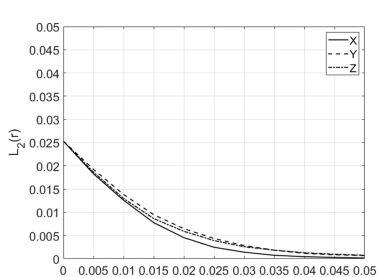

P-0.25+A-1-Top

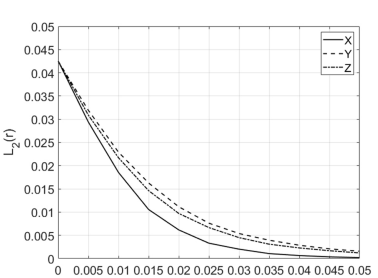

P-0.25+A-1-Middle

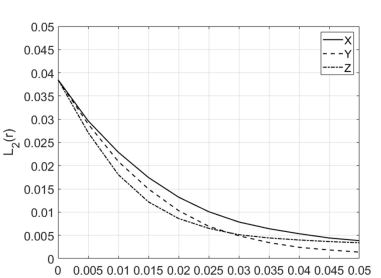

P-0.25+A-1-Bottom

Figure 14

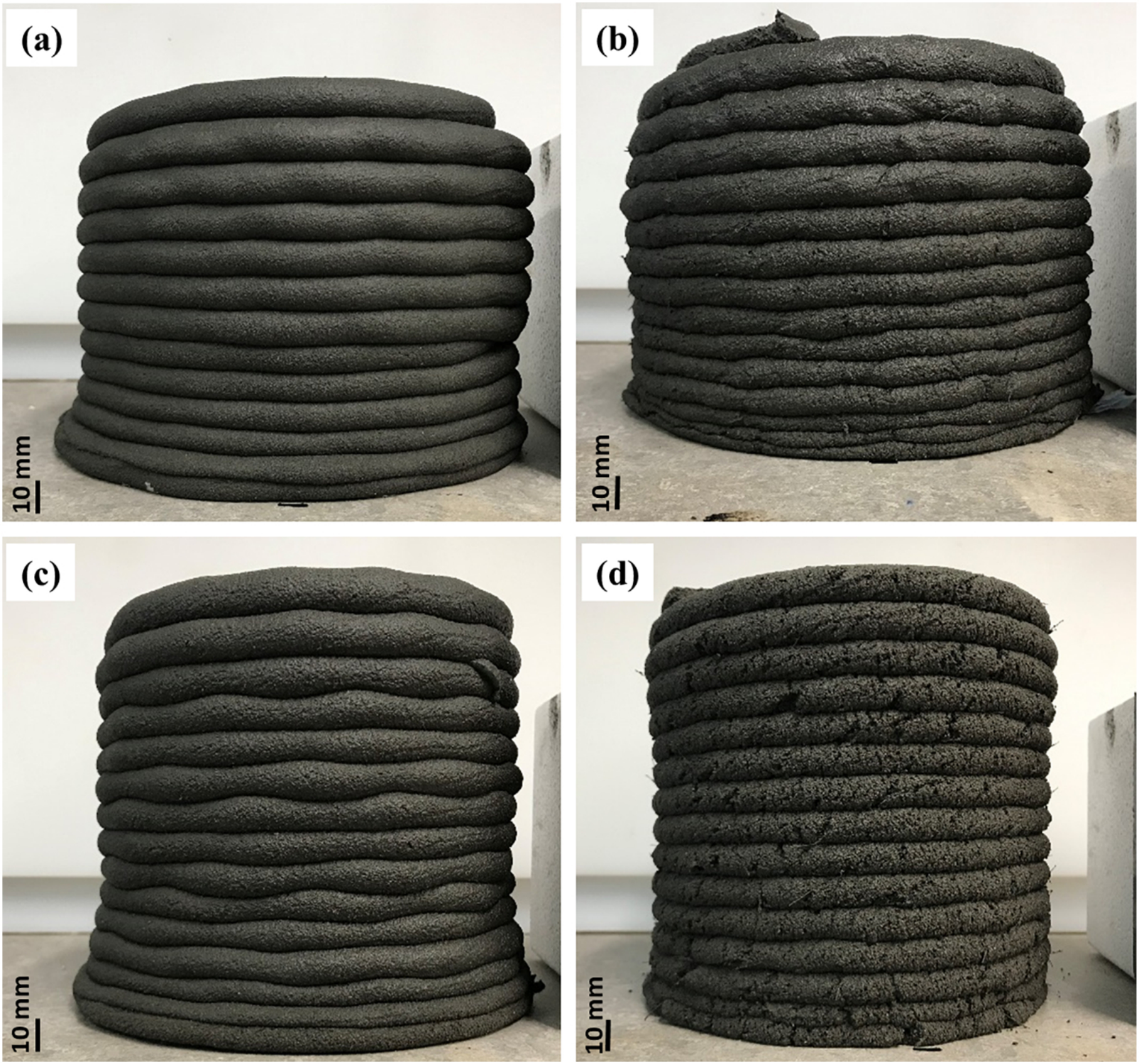

Figure 15